Geometry and kinematics of the Middle to Late Miocene salt tectonics, central Egyptian Red Sea margin

Moamen Ali [a,b,c], Hemin Koyi [a,d,*], William Bosworth [e], Marco Ligi [f], Philip J. Ball [g], Alessandro Decarlis [a,b]

[a] Department of Earth Sciences, Khalifa University of Science and Technology, Abu Dhabi, United Arab Emirates
[b] R.I.C.H. Center: Research and Innovation on CO_2 and H_2, Khalifa University of Science and Technology, Abu Dhabi, United Arab Emirates
[c] Department of Geology, Assiut University, Assiut, Egypt
[d] Hans Ramberg Tectonic Laboratory, Department of Earth Sciences, Uppsala University, Sweden
[e] Apache Khalda Corp LDC, 11 Street 281, New Maadi, Cairo, Egypt
[f] Istituto di Scienze Marine, CNR, Via Gobetti 101, 40129, Bologna, Italy
[g] Keele University, Faculty of Natural Sciences, Geography, Geology and the Environment, William Smith Building, Newcastle, ST5 5BG, UK

ARTICLE INFO

ABSTRACT

The Red Sea basin includes a thick Middle to Late Miocene evaporitic succession that underwent halokinesis and caused intensive reshaping of the seafloor and the development of salt-tectonic structures. However, the geometry and kinematics of these structures are still poorly understood. This study uses 2D and 3D seismic surveys and well data of the northern Egyptian Red Sea to systematically describe the distribution and morphology of salt structures, discuss their initiation, and construct a kinematic model for their origin. Our results indicate that the massive salt layer developed into five major NW-SE to NNE-SSW trending salt walls, characterized by relatively irregular crests and moderately dipping flanks. In addition, several symmetrical and asymmetrical folds and two categories of normal faults (subsalt and suprasalt) have been recognized. Based on our observations, salt mobilization in the study area started in the Late Miocene, during the precipitation of layered evaporites, and continued until the present day. In the northern Egyptian Red Sea, seismic interpretation indicates that halokinesis was triggered by a combination of thin- and thick-skinned systems, where the latter played a major role. The salt layer was welded during the Quaternary as several sags and grabens developed above the salt diapirs. Thick-skinned physical models are compatible with our observations, supporting the impact of basement faulting on Red Sea diapirism.

1. Introduction

The Red Sea rifting is a relatively young extensional system. The Nubian and Arabian shields in the conjugate margins have been separating since the Late Oligocene-Early Miocene (e.g. McKenzie et al., 1970; Burke and Dewey, 1973). GPS data show that the rifted margins are diverging at different rates from south to north, as the southern Red Sea is extending about 17 ± 1 mm/yr, while the extension rate in the northern Red Sea is only 7 ± 1 mm/yr (ArRajehi et al., 2010). Initially, the extension direction of the Red Sea was N65°E–S65°W, orthogonal to the rift axis. Subsequently, when the northern plate boundary of Arabia shifted from the Gulf of Suez to the left-lateral Dead Sea transform (~14-12 Ma), the extension direction in the northern Red Sea shifted

from orthogonal to oblique, with a general NNE trend parallel to the Dead Sea Transform (Lyberis, 1988; Bosworth et al., 2005; ArRajehi et al., 2010). The transition from a continental to an oceanic crust occurred only in the southern and central sectors of the Red Sea (Bonatti et al., 1984; Bonatti, 1985; Ligi et al., 2012). Evidence for continuous or punctuated seafloor spreading has been found with the recovery during marine surveys of basaltic rocks with mid-ocean ridge (MORB) affinity at different sites along the axis between 17° N and 19° 30′ N (Fig. 1a; Girdler and Whitmarsh, 1974; Bonatti, 1985). Based on magnetic anomalies, some authors have estimated an age of 5 Ma for the inception of the oceanic crust in the southern Red Sea (Cochran, 1983; Bonatti, 1985; Schettino et al., 2016; 2019). In the central sector, some axial deeps (Thetis and Nereus) were interpreted as isolated ridge segments
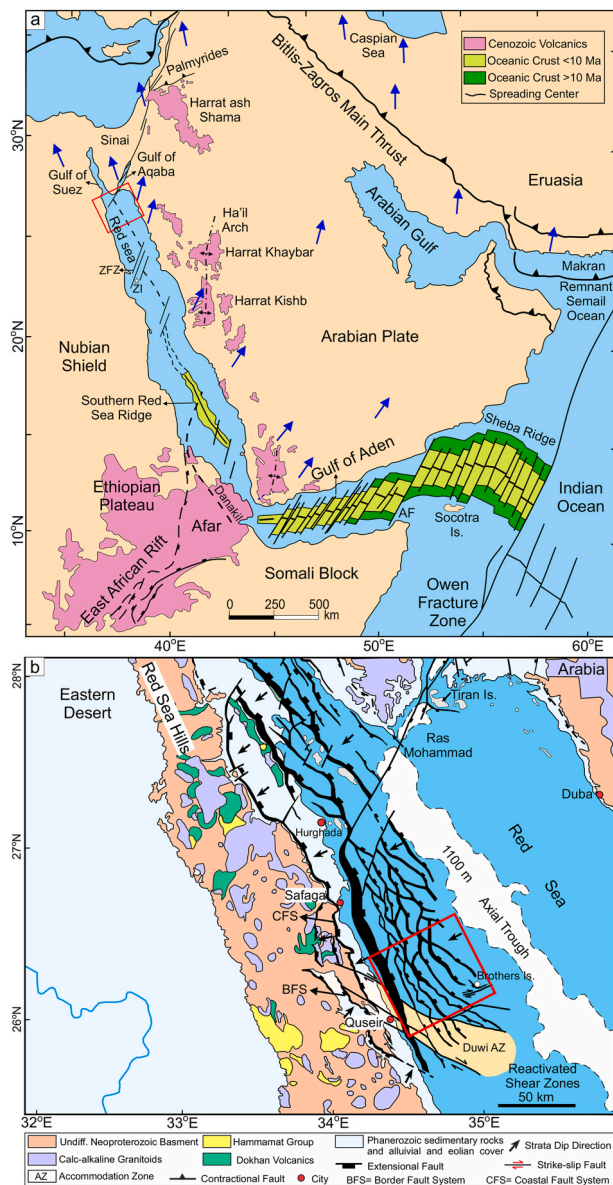
---

* Corresponding author. Hans Ramberg Tectonic Laboratory, Department of Earth Sciences, Uppsala University, Sweden.
  E-mail address: hemin.koyi@geo.uu.se (H. Koyi).

Fig. 1. (a) Plate tectonic setting of the Red Sea, Gulf of Aden, Gulf of Suez, and Gulf of Aqaba. Modified from Hempton (1987), Khalil and McClay (2002), and Bosworth et al. (2005). Blue arrows denote plate movement directions after Mahmoud et al. (2005) and ArRajehi et al. (2010). ZI is Zabargad Island, ZFZ is Zabargad Fracture Zone, and AF is Alula-Fartak Fracture Zone. (b) Geological map of the northern Red Sea showing the main structural elements (modified from Bosworth et al., 2017). The red box represents the study area. (For interpretation of the references to colour in this figure legend, the reader is referred to the Web version of this article.)

and consist of 3 to 1 Ma old oceanic crust (Ligi et al., 2012; 2018).

Most of the controversies about the northern Red Sea rifting evolution (Masini et al., 2020; Le Magoarou et al., 2021; Ali et al., 2023) are due to the limited access to good data caused both by industrial disclosure policies and by technical limitations on seismic images imposed by the presence of evaporites. Both rift evolution and the crust's nature are unclear (Sultan et al., 1992; Bosworth et al., 1993; 2020; Colombo et al., 2014; Le Magoarou et al., 2021). Several studies have proposed that the northern Red Sea is underlain by oceanic crust (Girdler and Underwood, 1985; Gaulier et al., 1988; Augustin et al., 2021; El Khrepy et al., 2021). For example, Augustin et al. (2021) built a model for the Red Sea using vertical gravity gradient (VGG) and earthquake and bathymetry data. They suggested that the oceanic crust exists in the

entire Red Sea, and the seafloor spreading was initiated at 13.5 and 12.8 Ma in the central and northern Red Sea, respectively. Conversely, other studies suggested that the northern Red Sea is a region of hyper-extended, thinned continental crust punctuated by several volcanic deeps distributed along the axis (Cochran, 1983, 2005; Bonatti, 1985; Bosworth et al., 1993; Mahsoub et al., 2012; Mitchell and Park, 2014; Almalki et al., 2015b; Le Magoarou et al., 2021). Ali et al. (2023) used several geophysical datasets and applied 2D forward modeling to study the nature of the crust in the central part of the northern Red Sea. They investigated a scenario where an exhumed lower continental crust or serpentinized mantle is present. Their results suggested that the best fit between the calculated and predicted gravity and magnetic data was obtained by including a limited mantle exhumation at the rift axis.

3D seismic and borehole data are commonly used to analyze the salt structures in sedimentary basins (e.g. Fiduk and Rowan, 2012; Jackson et al., 2015; Rojo and Escalona, 2018). The presence of the Middle to Late Miocene salt layer in the Red Sea represents an important factor in the formation of structural traps, controlling the distribution of reservoirs and source rocks and influencing hydrocarbon migration (Beydoun, 1989; Beydoun and Sikander, 1992; Nilsen et al., 1995; Alsharhan and Salah, 1997). In the last five decades, 14 exploratory boreholes were drilled in Egyptian waters. However, no productive field has been discovered, and the distribution of reservoir and source rocks within the margin is poorly understood (Gordon et al., 2010). In the Saudi Arabian and Yemeni margins, several previous studies focused on detailing the presence of salt bodies (Richter et al., 1991; Heaton et al., 1995; Orszag-Sperber et al., 1998; Mohriak, 2019), salt geometry, and the direction of salt flow (Colombo et al., 2014; Rowan, 2014; Almalki et al., 2015a; Feldens and Mitchell, 2015; Mitchell et al., 2017; 2019; 2021; 2022; Muzaffar et al., 2018; Smith and Santamarina, 2022). The data utilized included 2D seismic profiles, Bouguer gravity anomalies, bathymetry, marine magnetotellurics, gravity gradiometry, and controlled-source electromagnetics (Mart and Ross, 1987; Orszag-Sperber et al., 1998; Mitchell et al., 2010; 2021; Colombo et al., 2014; Rowan, 2014). A controversial issue regarding salt has been the interaction of the salt with the postulated oceanic crust in the Red Sea. High-resolution bathymetry images have shown allochthonous salt masses travelling along the seabed. This model has been used as an analogue for other margins (e.g. Angola and Brazil; Mohriak, 2014; Feldens and Mitchell, 2015). Despite these studies, the geometry and kinematics of the Middle to Late Miocene salt structures are still poorly understood partly because none of these previous studies have provided a 3D or temporal understanding of the diapirs along the Egyptian margin. In this study, we use 2D and 3D seismic and borehole data from the central part of the Egyptian Red Sea (offshore Quseir) and cross-section reconstructions to study the initiation and evolution of the salt structures. We construct two–way time (TWT) and isopach maps of the massive salt layer, layered evaporites, and Pliocene-Quaternary sediments and use these to provide a systematic description of the distribution and morphology of salt bodies, intra-salt structures, and their ultimate structural variabilities. We also identify the main basement-involved faults penetrating the base of the salt reflection and those affecting the overburden sediments, constrain the relative age of the salt movement, and determine the kinematic scenario that best fits the observed structural styles.

2. Geological setting of the northern Red Sea

The Egyptian margin contains numerous km-scale tilted blocks bounded by major NW-SE trending normal faults generally parallel to the Red Sea rift axis (Fig. 1; e.g. Barakat and Miller, 1984; Montenat et al., 1988; Patton et al., 1994; Khalil and McClay, 2001). The onshore stratigraphy of the northern Red Sea was described in detail by different studies (Jarrige et al., 1990; Bosworth et al., 1998; 2020; Khalil and McClay, 2009), while the offshore type-succession (Fig. 2) has been studied using the few available commercial well data (Fig. 3; Miller and
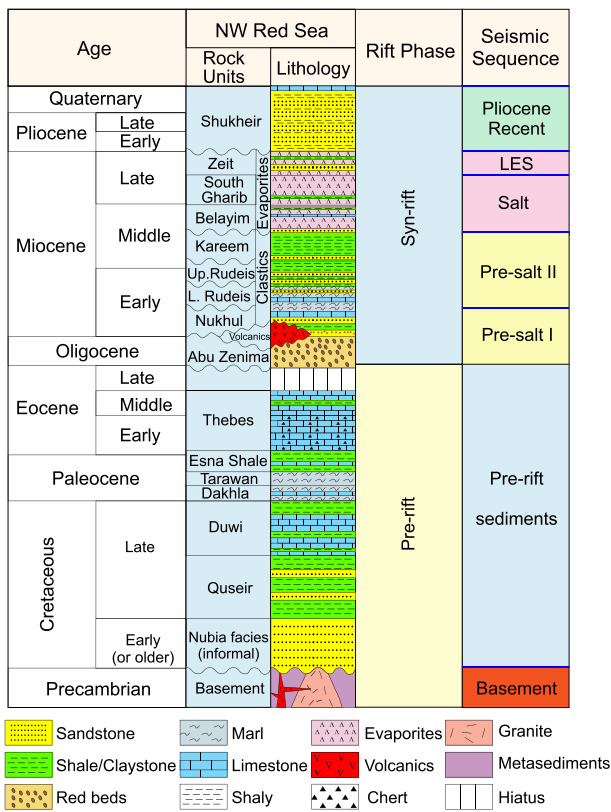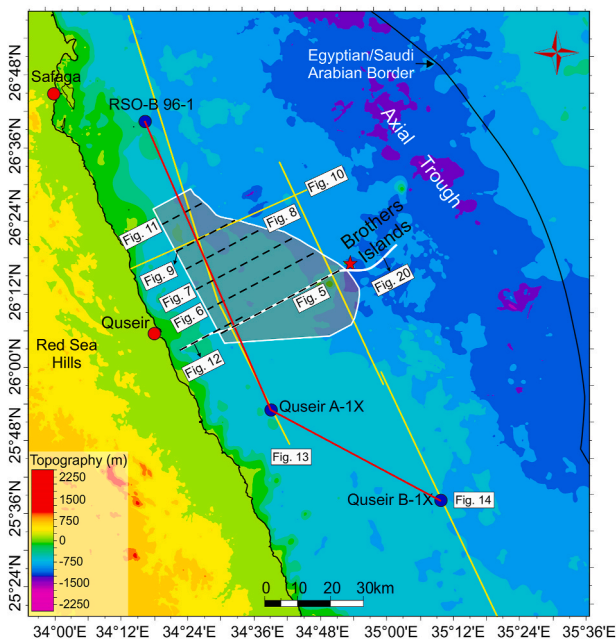
Fig. 2. Stratigraphic column of the offshore northern Red Sea (modified from Bosworth et al., 2020; Moustafa and Khalil, 2020). Blue lines denote the interpreted seismic horizons. (For interpretation of the references to colour in this figure legend, the reader is referred to the Web version of this article.)

Fig. 3. Bathymetric map of the central part of the Egyptian rifted margin, and location of wells and seismic sections used in this study. The shaded area indicates the available 3D seismic survey. The dashed black lines represent the interpreted crosslines. Yellow lines show location of 2D seismic profiles, and blue points indicate location of wells used to tie with them. (For interpretation of the references to colour in this figure legend, the reader is referred to the Web version of this article.)

Barakat, 1988; Bosworth et al., 2020; Tewfik and Ayyad, 1982). The offshore geological record of the Egyptian Red Sea is divided into two main tectonostratigraphic sequences (Miller and Barakat, 1988): i) pre-rift, represented by igneous and metamorphic rocks and ii) syn-rift, which is divided into an early rift section assigned to the Nukhul Formation unconformably overlain by a main syn-rift section (Fig. 2). The main syn-rift sequence includes Early to Middle Miocene siliciclastic rocks (Rudeis and Kareem Formations) and Middle to Late Miocene massive salt layer and layered evaporites (Belayim, South Gharib, and Zeit Formations), followed by Plio-Quaternary clastic rocks (Fig. 2).
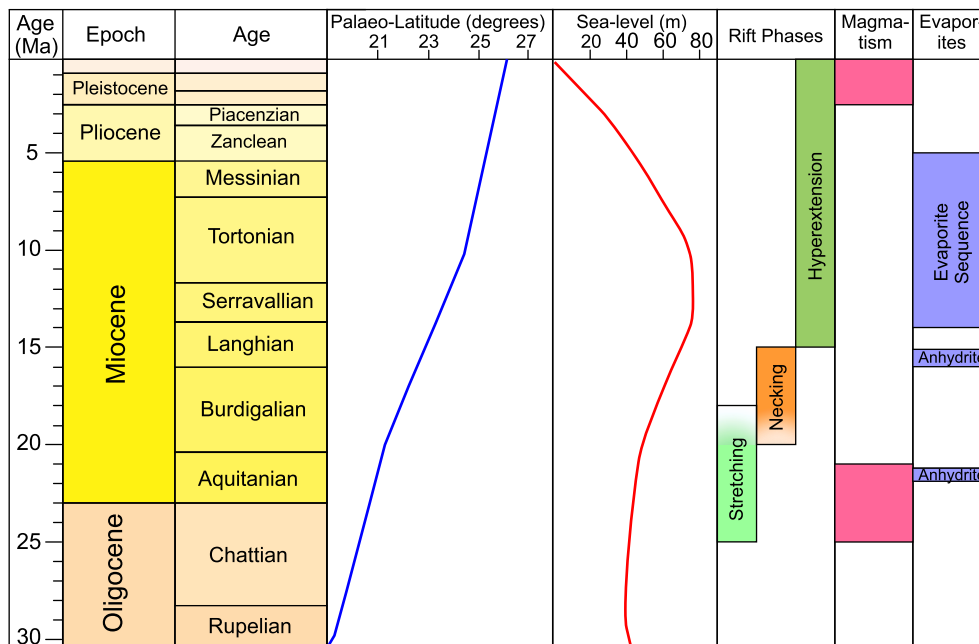
During the early Middle Miocene, the Aqaba-Levant transform boundary started accommodating the motion of the Arabian plate, resulting in a sharp change in the extension direction. As a consequence, the marine connection of the Red Sea to the Mediterranean Sea became restricted but not terminated, and the sedimentation in the Red Sea changed from open marine to evaporitic (Hughes and Johnson, 2005; Bosworth et al., 2005; Bosworth, 2015). Several authors suggest that the main evaporite sequence (Belayim, South Gharib, and Zeit Formations) was precipitated during the Middle-Late Miocene (e.g., Orszag-Sperber et al., 1998; Bosworth et al., 2005; Bosworth, 2015). The precipitation of the massive salt layer was associated with an arid period during the Late Serravallian-Tortonian, followed by a wet phase in the Messinian (Griffin, 1999; 2002). The Messinian episode, named the Zeit Wet Phase, was associated with a high rainfall time and deposition of the Zeit Formation and its equivalents (Fig. 2.). This formation is characterized by high clastic content compared to the underlying units. Furthermore, Smith and Santamarina (2022) suggested that the precipitation of thin halite and anhydrite beds within the layered evaporite sequence (Zeit Formation) is related to cyclic yet limited seawater recharge and multi-year drying periods of the Red Sea rifted margin. Ball et al. (2018) observed that salt appears to onlap onto exhumed lower crust or mantle rocks in Zabargad Island and along the Saudi Arabian margin, areas in which exhumation probably occurred at ~15-14 Ma (Fig. 4). Evaporite precipitation seems to be largely synchronous over the entire Red Sea and the Gulf of Suez, and likely occurred during a specific rifting stage corresponding to the transition from necking to hyperextension (Rowan, 2014; Ali et al., 2023). Ali et al. (2023) provided a detailed rift domain model for the northern Red Sea. They interpreted the necking zone close to the shoreline, which probably occurred in the Early Miocene due to the formation of an east-dipping detachment fault. The continental crust thinned significantly from 32 km beneath the onshore Quseir region to 22 km below the necking domain. The distal domain formed due to the hyperextension processes is found along the offshore Quseir section and is characterized by the deposition of the Middle to Late Miocene evaporite sequence where the thickness of the continental crust thinned to <10 km (Ali et al., 2023, their Fig. 10). The evaporitic sequence is intensively affected by salt tectonics, forming salt diapirs and salt walls separated by mini-basins filled by clastic rocks and evaporites (Mart and Ross, 1987; Colombo et al., 2014).

At the end of the Miocene, the entire Red Sea basin became subaerially exposed (Bosworth et al., 2005; Mitchell et al., 2017; 2021), and a major unconformity surface formed due to this event, which marks the top of the Zeit Formation and is identifiable in seismic reflection data, known as the S-reflector (Ross and Schlee, 1973; Mitchell et al., 2010). It is characterized by a low frequency and high amplitude seismic reflection resulting from the dramatic increase in velocity from ~2200 to 5000 m/s. This dramatic increase in seismic velocity is due to a thin anhydrite unit at the top of the Miocene evaporite, followed by poorly consolidated Pliocene clastic sediments (Colombo et al., 2014). Seafloor spreading initiation in the southern Red Sea, at ~5 Ma, caused the opening of a connection with the Indian Ocean through the Strait of Bab-el-Mandeb. This event enabled a new marine ingression from the south and determined the end of the evaporite precipitation in the basin (Mart and Hall, 1984; Mart and Ross, 1987).

The Middle to Late Miocene evaporite sequence was precipitated due to the evaporation of seawater occasionally entering into the

Fig. 4. Summary scheme showing rift episodes and the deposition time of the evaporites, as well as the magmatism stages in the northern Red Sea, modified after Ali et al. (2023). Sea-level curve from Haq and Schutter (2008) and Paleo-latitudes from van Hinsbergen et al. (2015). (For interpretation of the references to colour in this figure legend, the reader is referred to the Web version of this article.)

hydrographically semi-isolated Red Sea Basin. It is identified as basin-wide marine evaporites, resulting from a combination of hydrological and tectonic circumstances (Warren, 2010). Smith and Santamarina (2022) suggested that the salt precipitation in the Red Sea was controlled by the recharge rate of the seawater through the Bab-el-Mandeb Strait. The formation of a 1 km thick salt layer resulted from the evaporation of 53 km of Red Sea seawater. On the contrary, Hovland et al. (2015) provided a new model (hydrothermal salt model) where they assumed that the Red Sea's evaporite sequence formed due to the hydrothermal circulation of seawater.

Several previous studies suggested that the Red Sea salt was mobilized dominantly by thin-skinned gravitational failure, with proximal extension and distal contraction (Heaton et al., 1995; Rowan, 2014; Tubbs et al., 2014). On the other hand, the presence of alluvial fans and carbonate platforms parallel to the current coastline is interpreted as the dominant component of nearshore salt movement in the central and southern Red Sea (Smith and Santamarina, 2022). Mart and Ross (1987) postulated that the high thermal gradient, caused by highly attenuated crust and underlying ascending mantle, may have triggered salt diapirs structures. The salt diapirs observed by Mart and Ross (1987) in the northern Red Sea have a NW-SE trend with an average length and width of 30 and 4 km, respectively.

3. Data and methods

2D and 3D seismic surveys and borehole data have been used to study the geometry and kinematics of the Middle to Late Miocene salt structures in the central part of the Egyptian margin (Fig. 3). The 3D seismic survey was acquired by British Gas in 1999 and covers 1600 km² offshore Quseir province between 26 and 26° 25′ N (Fig. 3; Gordon et al., 2010). It consists of 1729 NW-SE in-lines with a line spacing of 25 m and 4879 NE-SW cross-lines with 12.5 m spacing. Time-migrated seismic data allow imaging up to 7 s TWT. Furthermore, six 2D seismic profiles with a total length of ~471 km were used. The seismic profiles were acquired by Philips and Esso Red Sea between 1975 and 1977 with vertical seismic recording of 6 and 5 s TWT, respectively. Three wells that penetrated the Precambrian basement (granite, granodiorite and gabbro) are used to tie seismic data: Quseir B-1X, Quseir A-1X, and

RSO-B 96–1 (Fig. 3). The RSO-B 96–1 was drilled by Esso Red Sea in 1980 reaching a total depth of 4258.08 m from water surface; Quseir B-1X and Quseir A-1X wells were drilled by Philips Red Sea between 1977 and 1978 to a total subsea depth of 4213.86 m and 5038.34 m, respectively.

Seismic interpretation procedures accounted for seismic-to-well ties, fault interpretation, and seismo-stratigraphic units picking offshore Quseir, constructing TWT and isopach maps for the salt layer, layered evaporites, and post-evaporitic sediments using the Schlumberger Petrel™ software (e.g. Ali et al., 2018; 2020). Six horizons and five seismic sequences (Plio-Quaternary, layered evaporites, transparent evaporites, Pre-salt II, Pre-salt I, and basement) were interpreted picking the upper limit of each formation based on well data, regional continuity, and amplitude of the seismic reflections. The top surface of the Plio-Quaternary sequence and layered evaporites was interpreted for every single crossline and inline with high confidence, using a 3D auto-tracking tool. Concurrently, the interpretation of the other horizons was done manually every 50 crosslines and inlines with some uncertainties. The ages of selected seismic units are taken from previous lithostratigraphic studies of the northern Red Sea (Hughes and Beydoun, 1992; Bosworth et al., 1998; Hughes and Johnson, 2005; Khalil and McClay, 2009). The major phases of salt flow were determined based on identifying growth strata, toplap, onlap, downlap, and truncation surfaces (Figs. 5–13). The RMS amplitude was applied to the 3D seismic cube to delineate the boundary of the salt walls in the time domain. Six time slices have been extracted at TWT values between 1.2 and 2.5 s. Depth-converted structural reconstructions were made based on interpreted seismic surveys to estimate the progressive evolution of the salt diapirs. The last 20 km in the southwestern part of the geological model is constructed based on the seismic interpretation in Fig. 5 of Ali et al. (2023). Time-to-depth conversions were performed by adopting an average velocity value for each seismic sequence (Table 1; Gaulier et al., 1988; Makris and Rihm, 1991; Rihm et al., 1991; Saleh et al., 2006; Ligi et al., 2018). Due to the difficulty in determining the exact timing of fault movement and displacement amount, the extension and shortening values in the reconstructions have some uncertainties.
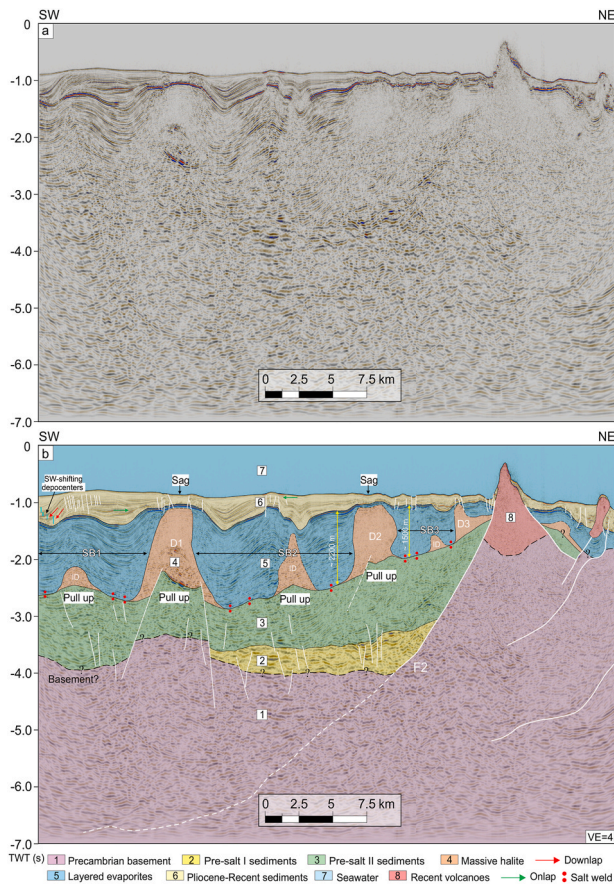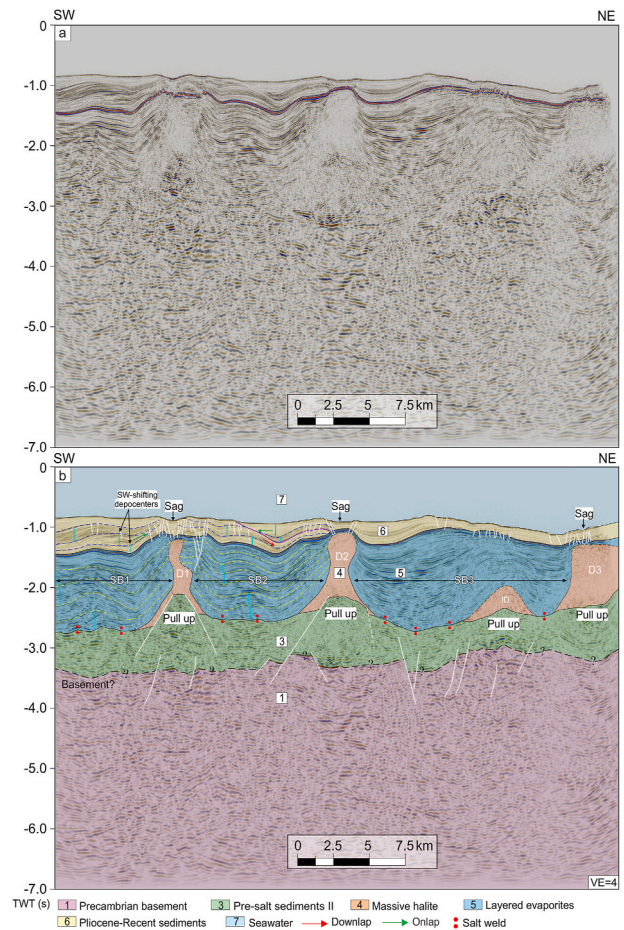
Fig. 5. (a) Uninterpreted and (b) Interpreted crossline 3200, depicting pre-salt sediments and salt diapirs. D1 salt diapir roots to a narrow horst. Note two Quaternary volcanoes on the northeastern side of the profile. White lines indicate normal faults. D, ID, and SB denote diapir, immature diaper, and subbasin, respectively. Section location is shown in Fig. 3. VE: vertical exaggeration.

Fig. 6. (a) Uninterpreted and (b) Interpreted crossline 3900, displaying extensional faults (white lines), mature (D) and immature (ID) salt structures, and unconformity surface above the layered evaporites. SB denotes subbasin. Section location is shown in Fig. 3. VE: vertical exaggeration.

4. Results

4.1. Seismic stratigraphy

Six seismic crosslines from the 3D seismic survey and three 2D seismic lines (Figs. 5–13) were interpreted to highlight the main structures (subsalt and suprasalt faults, seismic units, and salt diapirs). Interpreting the top of the basement was challenging due to the thick, overlying evaporite section. However, a continuous high-amplitude seismic reflection in the shallow domain was interpreted as the top of the basement (Fig. 10). Well-control added some confidence to this interpretation, even in the deepest part of the study area. In the time domain, the basement is easily recognizable at a depth of 1 s TWT in the slope area (Fig. 10) to ~4.5 s further offshore with some uncertainties (Fig. 13). The basement is uplifted in the central part of the offshore Quseir, where it is cut by a set of normal faults forming two major structural highs (Figs. 5 and 10). Furthermore, two basement highs reaching the seafloor (Fig. 5) were recognized in the northeastern part.

The subsalt sediments are divided into two seismo-stratigraphic units: Pre-salt I and Pre-salt II (Figs. 5 and 8). The Pre-salt I sequence unconformably overlays the basement and is restricted to the deepest parts of the southeastern and central segments of the study area. The Pre-salt I is approximately 0.1–0.7 s thick (150–900 m) and contains flat-lying to sub-horizontal, moderately layered, high-amplitude reflections (Figs. 5 and 8). The Pre-salt II was unconformably deposited above the crystalline basement in most of the offshore Quseir; however, it is locally found conformably above the Pre-salt I. This sequence is characterized

by low to moderate amplitude and moderately to well-layered reflections (Figs. 5–13). The Pre-salt II facies display large thickness variation ranging from 0.15 to 1.5 s TWT (ca. 200–2100 m). Seismic profiles also show that the Pre-salt II was not deposited in the basin flanks, offshore the modern Egyptian coast (Figs. 10–12).

Evaporitic rocks are grouped into two main sequences; seismically "transparent" evaporites (massive salt) overlain by layered evaporites (Figs. 5–13; Izzeldin, 1987; Colombo et al., 2014; Mitchell et al., 2017; Ali et al., 2023). The base and top surfaces of the massive salt layer display strong reflections with high amplitudes, whereas internally, the unit is chaotic with low-amplitude reflectivity. The salt interval is widely distributed in the distal margin but not recorded towards the coast (Figs. 10 and 12). Three main subbasins have been recognized between the main salt structures (Figs. 6 and 10), consisting of thick sedimentary successions of layered evaporites and Plio-Quaternary sediments. These mini-basins are labelled southwestern subbasin (SB1), central subbasin (SB2), and northeastern subbasin (SB3) (Figs. 5 and 6). Northeast of the basement structural highs, the salt sequence becomes thin, characterized by poorly defined layering and low amplitude reflections, and salt structures disappear (Fig. 5).

The layered evaporites unit consists of continuous, moderately to well-stratified seismic reflections with moderate to high amplitude intercalated with continuous and low amplitude reflections (Figs. 5–13). In the western sector of the offshore Quseir, the seismic reflections of the layered evaporites downlap on the salt layer and the basement (Figs. 10–12). In the southwestern mini-basin (SB1), the layered evaporites are characterized by inclined reflections dipping southwest and
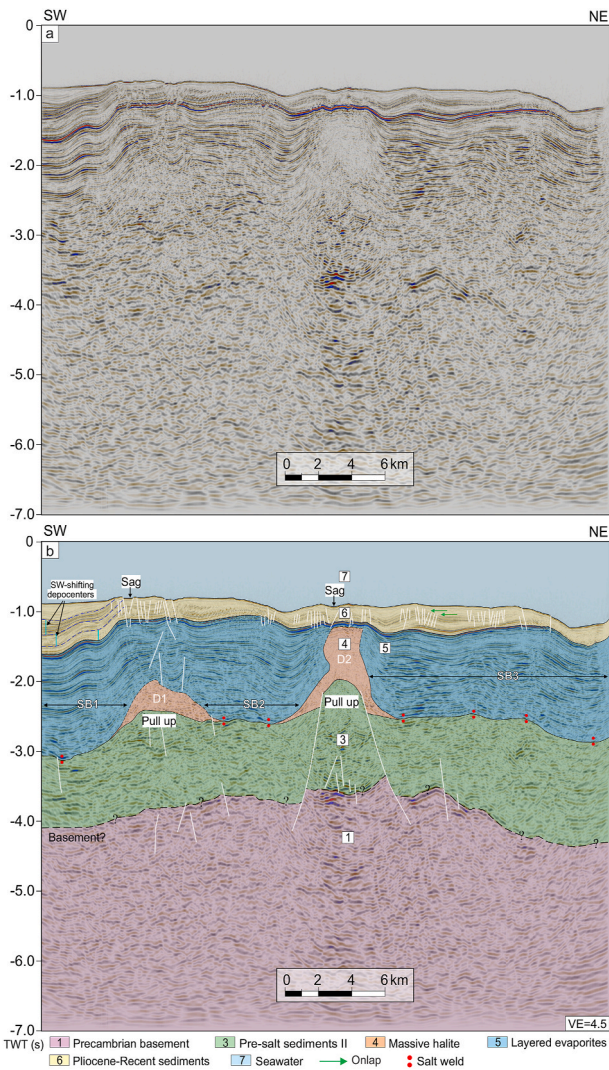
Fig. 7. (a) Uninterpreted and (b) Interpreted crossline 4450, crossing the central part of the offshore Quseir in a NE-SW. The section shows a major horst, two salt diapirs, and many subsalt and suprasalt faults (white lines). D and SB denote diapir and subbasin, respectively. Section location is shown in Fig. 3. VE: vertical exaggeration.

Fig. 8. (a) Uninterpreted and (b) Interpreted crossline 5000, displaying extensional faults (white lines), salt structures, and depocenters migration of the Plio-Quaternary sediments. D and SB denote diapir and subbasin, respectively. Section location is shown in Fig. 3. VE: vertical exaggeration.

northeast with moderate thickening towards the southwest (Fig. 12). The central subbasin (SB2) shows slight width variations, ranging from 9 km to 11 km (Figs. 5, 6, 8 and 10). The subsalt faults controlled the deposition of the layered evaporites, as the unit moderately thickens toward the southwest in most of the interpreted seismic profiles (Figs. 5–7 and 9-11), except in the central area where it thickens in the opposite direction (Fig. 8). The layered evaporites are characterized by seismic reflections dipping southwest and northeast within the northeastern subbasin (SB3) and show discordant relationship with the salt diapirs (Figs. 6 and 10). This seismic sequence displays a moderate thickness variation in the SB3, expressed by a small SW thickening in the southeastern sector of the offshore Quseir (Fig. 6) and a SW thinning in the northwestern sector (Fig. 10). The layered evaporites contain several growth seismic sequences, characterized by southwestward shifting depocenters (Figs. 6 and 12). In addition, sedimentary features like angular unconformity, downlap, and truncated toplap closures are recognized in the lower part of the layered evaporite interval (Fig. 11). The top reflection of the layered evaporites is obvious and shows very high amplitude, representing an unconformity surface between the interbedded evaporites and Pliocene sediments (Fig. 5). Several normal faults with small to medium offset cut the upper part of the layered
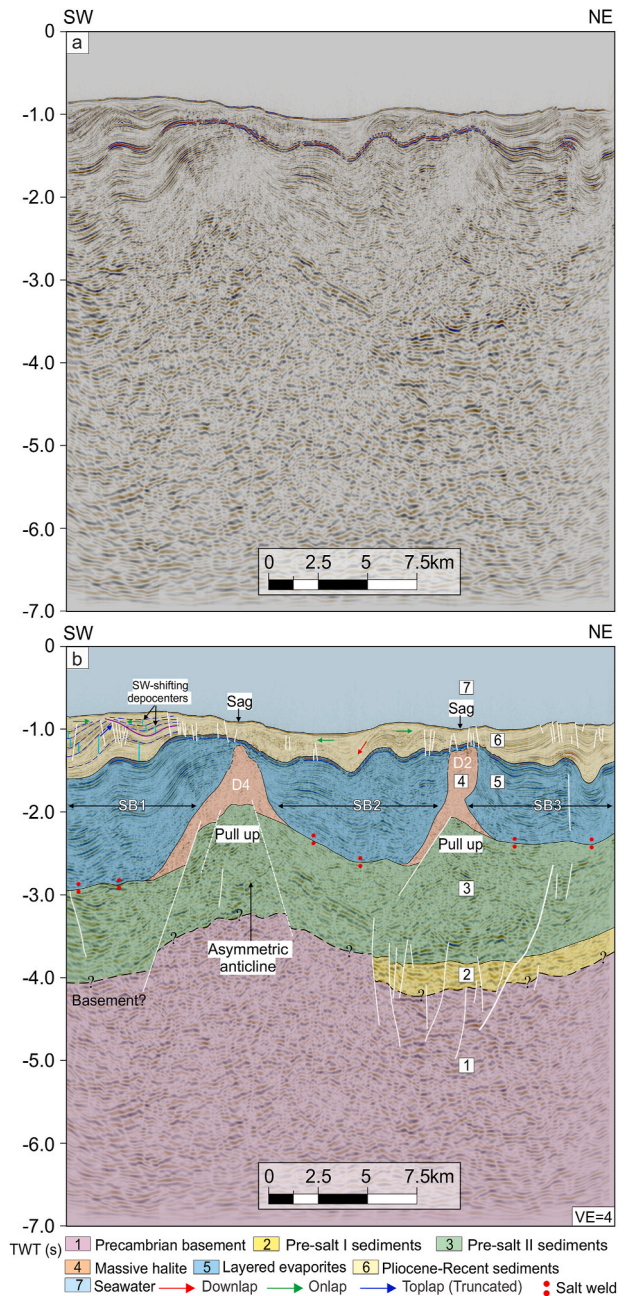
evaporites (Figs. 5–13).

The layered evaporites are unconformably overlain by the Plio-Quaternary sequence, representing the youngest sedimentary unit identified in the northern Red Sea. This sequence was deposited over the entire study area, including onshore (Fig. 5; Khalil and McClay, 2002, 2009), and consists of well-stratified, medium to high amplitude seismic reflections. The salt diapirs do not intrude on the Plio-Quaternary sequence (Figs. 5–13). Generally, growth seismic sequences are observed within the basins, showing prominent depocenters that shift towards the southwest (Figs. 6 and 8). In the southwestern subbasin (SB1), at least three major sedimentary cycles separated by truncation surfaces are observed within the Plio-Quaternary sequence (Fig. 12). Several minor normal faults with steep to moderate dip angle and low offset are recognized within this sequence (Figs. 5–13).
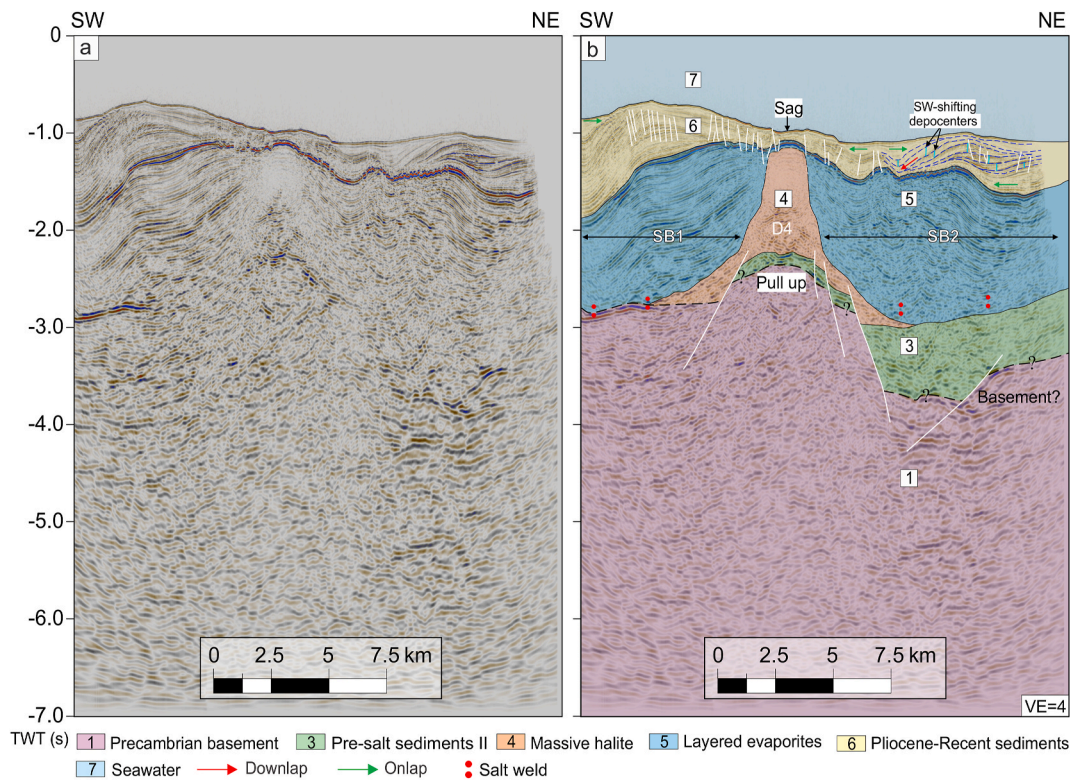
Fig. 9. (a) Uninterpreted and (b) Interpreted crossline 5500, depicting normal faults (white lines), a salt diapir (D), and depocenters migration of the Plio-Quaternary sequence. SB denotes subbasin. Section location is shown in Fig. 3. VE: vertical exaggeration.
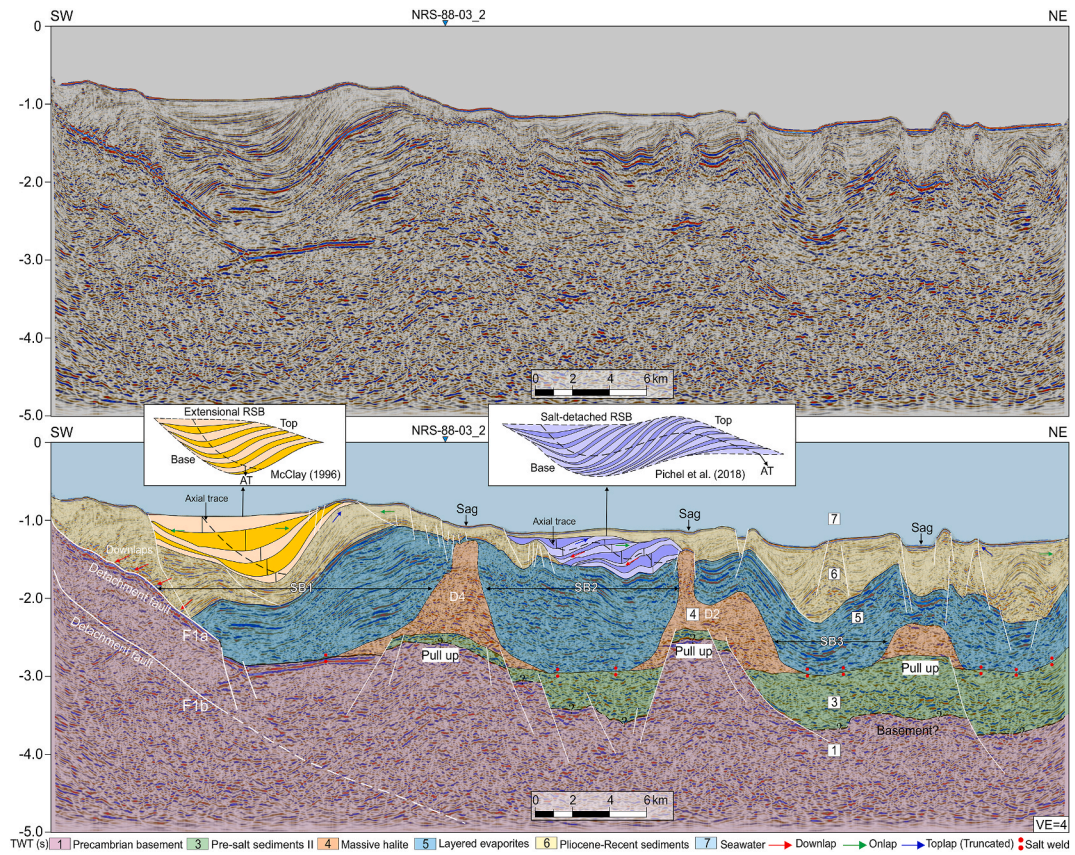
Fig. 10. (a) Uninterpreted and (b) Interpreted NE-SW seismic profile, passing through the margin. The section shows shallow and deep detachment faults, D1 and D2 salt diapirs root to narrow horsts, and two different types of ramp-syncline basins. White lines and SB denote normal faults and subbasin, respectively. Section location is shown in Fig. 3. VE: vertical exaggeration.
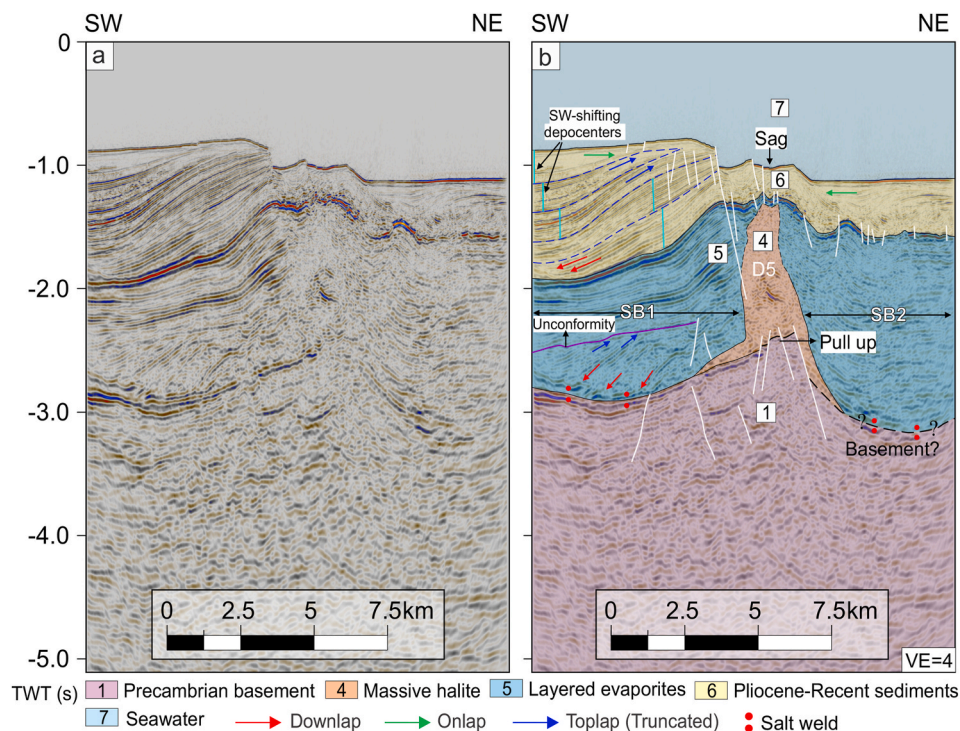
Fig. 11. (a) Uninterpreted and (b) Interpreted crossline 6300, showing a salt diapir (D) and normal faults (white lines). Note that the larger throw of the northeastern basement fault compared to the southwestern fault results in a large thickness variation in the overburden on both sides of the D5. SB denotes subbasin. Section location is shown in Fig. 3. VE: vertical exaggeration.

4.2. Well stratigraphy and correlation

Fig. 14 displays the correlation of three wells along a NW-SE direction from RSO-B 96–1 in the northwest to Quseir B-1X in the southeast of the study area (Fig. 3). The available well data indicate that the siliciclastic syn-rift sequence corresponds to three formations (Nukhul, Rudeis, and Kareem). The Nukhul Formation is recorded only in RSO-B 96–1 well with a total thickness of ~52 m and mainly includes sandstone. The Rudeis Formation is composed of claystone intercalated with thin sandstone and limestone interbeds. Its thickness varies from ~1685 m in the RSO-B 96–1 well to ~1805 m in the Quseir A-1X (Figs. 3 and 14). The Kareem Formation represents the upper part of the pre-salt sequence in the northern Red Sea. It is formed by claystone, siltstone, and sandstone interlayered with thin beds of calcareous limestone and dolostone. The Kareem Formation shows a slight thickness variation between 138 m at Quseir A-1X to 142 m at RSO-B 96–1 (Fig. 14).

The evaporite sequence corresponds to three formations: Belayim, South Gharib, and Zeit. The Belayim Formation mainly consists of anhydrite and halite interlayered with dolostone, calcareous limestone, and siltstone. Its thickness varies from 92 to 97 m in the Quseir A-1X and RSO-B 96–1 wells, respectively. The South Gharib Formation represents the main massive salt layer in Quseir offshore and shows a dramatic thickness variation ranging from 245 m at RSO-B 96–1 to 3225 m at Quseir B-1X (Fig. 14). It is composed of massive halite intercalated with thin beds of anhydrite. The Zeit Formation includes halite and anhydrite with sandstone, siltstone, and claystone interlayers. The thickness of the Zeit Formation significantly changes between 1115 and 1762 m in the RSO-B 96–1 and Quseir A-1X wells, respectively. However, it is not recorded in Quseir B-1X (Fig. 14). The Plio-Quaternary sequence (Shukheir Formation) is formed by sandstones with thin siltstone and claystone interbeds. Its thickness ranges from 180 m at RSO-B 96–1 to 316 m at Quseir B-1X (Fig. 14).

4.3. Geometry and regional distribution of salt diapirs

Seismic data show that, in the study area, the seismically "transparent" evaporite layer forms five major diapiric walls and three immature diapirs, disappearing toward the northwest (Figs. 5 and 6). The major and more mature salt diapiric walls are labelled D1, D2, D3, D4 and D5 (Figs. 5–11). Most of the salt walls have relatively irregular crests and moderately-dipping flanks. They are NW striking in the southeastern region of the offshore Quseir and NNW to NNE in the northwestern region (Supplementary Video 1). Salt walls are characterized by a slight discordance with the overburden beds and contractional anticlines with uplifted and eroded crests (e.g., Figs. 5 and 6). The geometry of salt walls changes along the strike. The D1 structure has a total length of ~31 km and narrows upward from ~4.3 km at the base to ~1.4 at the neck (Figs. 15 and 16). The height of the wall varies from 0.8 s TWT (~1700 m) to the northwest to 1.2 s TWT (~2500 m) in the southeast (Fig. 15). Salt wall D2 is the longest structure in the offshore Quseir with a total length of approximately 46 km (Figs. 15 and 16). It has an average width of 5 km at the base, and 1.5 km at the crest, and its height increases from 0.6 s TWT (~1250 m) in the northeast to1.2 s TWT (~2500 m) in the central part (Figs. 15 and 16). In the southeastern sector of the offshore Quseir, a subcircular salt body (D3) is observed (Fig. 15). This salt body surrounds a recent volcanic edifice and has an average length and width of about 16 and 6 km, respectively (Figs. 5, 15 and 16; Ali et al., 2022a). Its thickness ranges between 0.3 and 0.8 s TWT (600–1700 m). Salt wall D4 is striking NNW to NNE, is 17 km long and ~2.3 km wide with an average thickness of about 0.9 s TWT (~1900 m) (Figs. 15 and 16). The seismic data only partly image D5, which shows an average width and thickness of 1.7 and 0.8 s TWT (~1700 m), respectively (Fig. 15).

Fig. 13 shows an interpreted 2D seismic section trending SSE-NNW with a total length of approximately 140 km. The seismic profile crosses obliquely (~25°) several salt walls. The interpreted seismic section displays five salt structures, two of which are also present in the central sector of the 3D seismic profiles (as described above, Fig. 13).
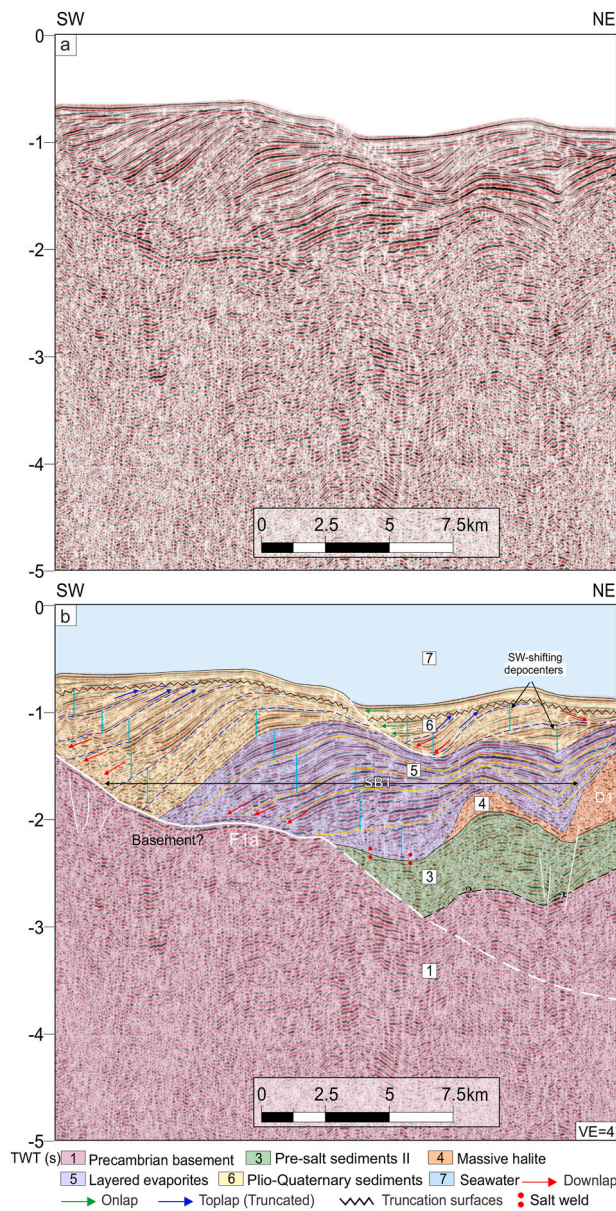
Fig. 12. (a) Uninterpreted and (b) Interpreted NE-SW seismic profile, passing through the southwestern part of the offshore Quseir. The section depicts depocenters' migration landwards and normal faults (white lines). D and SB denote diapir and subbasin, respectively. Section location is shown in Fig. 3. VE: vertical exaggeration.

The other three salt structures (D6, D7, and D8) were recognized in the NNW and SSE sectors of the seismic section. Salt structure (D6) is marked by very strong reflections at its top and base. It has a relatively flat crest and moderately dipping flanks, and an average thickness of about 0.8 s TWT (~1700 m; Fig. 13). Salt wall (D7) is located SSE of RSO B96-1 well, where the seismic section probably marginally cuts the salt structure. It is characterized by an irregular to triangular crest with a height of 0.6 s TWT (~1250 m; Fig. 13). Salt wall (D8) displays continuous high-amplitude reflections parallel to subparallel at its base and top (Fig. 13). The crest of D8 is relatively flat and the flanks are moderately steep (~45°), while the average thickness is about 1.2 s TWT (~2500 m).

4.4. Structural elements

Based on the interpreted seismic data, the main structural elements

in the offshore Quseir are normal faults and anticline and syncline folds (Figs. 5–13). Normal faults are classified into subsalt and suprasalt structures. The subsalt faults are rooted in the crystalline basement and cut through the entire subsalt sequence, with some of them displacing the base of the massive salt layer, creating horsts beneath the positions of the major salt diapirs (e.g. Figs. 9–11). The layered evaporites and post-evaporitic deposits appear to be unaffected by faults developed in the subsalt sediments, except for the master faults (Figs. 5, 10 and 20). The low-angle normal fault F1a occurs near the shoreline of the Egyptian margin. It dips to the northeast and displays a large vertical throw offsetting the basement by about 2.8 s TWT (Figs. 10 and 12). The true dip angle changes from ~25° at 1 s TWT to ~12° at 2.5 s (TWT). F1b fault dips to the northeast with a dip angle varying between ~25° at 1.7 s TWT and ~10° at 3.4 s (TWT) and cuts through the basement (Fig. 10). F2 is located in the southeastern part of the offshore Quseir and dies out northwestward. The true dip angle decreases from 45° near the seafloor to 15° at the top of the basement (Figs. 5 and 17).

Normal faults in the suprasalt sequence mainly affect the upper part of the layered evaporites and the Pliocene to recent sequence; however, a few are rooted at the top of the salt layer (Figs. 10 and 11). These faults dip northeast and southwest with moderate to high dip angles (~45°–75°), showing limited throws, usually a few tens of meters (Figs. 5–8). The offset of the suprasalt normal faults increases northwestward, where it may reach 200 m (Figs. 10 and 11). Moreover, the density of the suprasalt faults increases directly above the crests of the salt structures and decreases at the depocenters of the subbasins (Figs. 5–13).

Several anticline and syncline folds are imaged in the offshore Quseir (Figs. 5–13). They involve layered evaporites and the Pliocene to recent deposits (Fig. 17b and c). In the southern segment of the study area, symmetrical and asymmetrical synclines, separated by anticlines, are observed. They have moderately inclined limbs and typically trend NW-SE, parallel to the salt walls in this area (Figs. 5 and 17b and c). Lengths and amplitudes of the folds vary from about 7 to 45 km and 0.4–0.7 s TWT (~600–900 m), respectively, and have a wavelength of more than 6 km (Figs. 5 and 17b). The density and complexity of the recognized folds increase toward the northwest, where many of them (>20) were identified (Figs. 1, 8 and 17b). They are symmetric and asymmetric; however, the latter are more common and have gently to moderately inclined limbs. They are generally smaller than the structures in the southern sector of the offshore Quseir, where they reach an average length of about 5 km and an average amplitude and wavelength of 0.4 s TWT (600 m) and 5 km, respectively (Figs. 1, 8 and 17b). The folds typically trend from NNE-SSW to NE-SW, subparallel to the salt walls in this region (Fig. 17b).

4.5. TWT structural and isopach maps

TWT maps of the top of the Plio-Quaternary and layered evaporites sequences are shown in Fig. 17a and b, respectively. The TWT structural map of the top of the Plio-Quaternary sequence shows that the maximum depths are observed in the eastern and northeastern sectors, while the minimum values are distributed in the western and northwestern regions (Fig. 17a). Seafloor depth, expressed as TWT, ranges from 0.55 to 0.65 s (~425–500 m bsl) towards the present shoreline and from −1.2 to −1.35 s (~930–1050 m bsl) in the deepest sectors of the offshore Quseir (Fig. 17a). The time domain structural map of the layered evaporites exhibits a different pattern (Fig. 17b). In fact, the top of this sequence reaches the highest values, ranging from 2.0 to 2.1 s TWT (~2000–2100 m bsl), in the northwestern region of the offshore Quseir. In contrast, the shallow areas, controlled by the distribution of the underlying salt walls, form NW-SE elongated patterns. These regions display TWT values ranging from 0.9 to 1.1 s (900–1100 m bsl) and are separated by embayments reaching depths between 1.3 and 1.65 s (~1300–1650 m bsl; Fig. 17b). The structural setting of the offshore Quseir is mainly controlled by two major sets of extensional faults
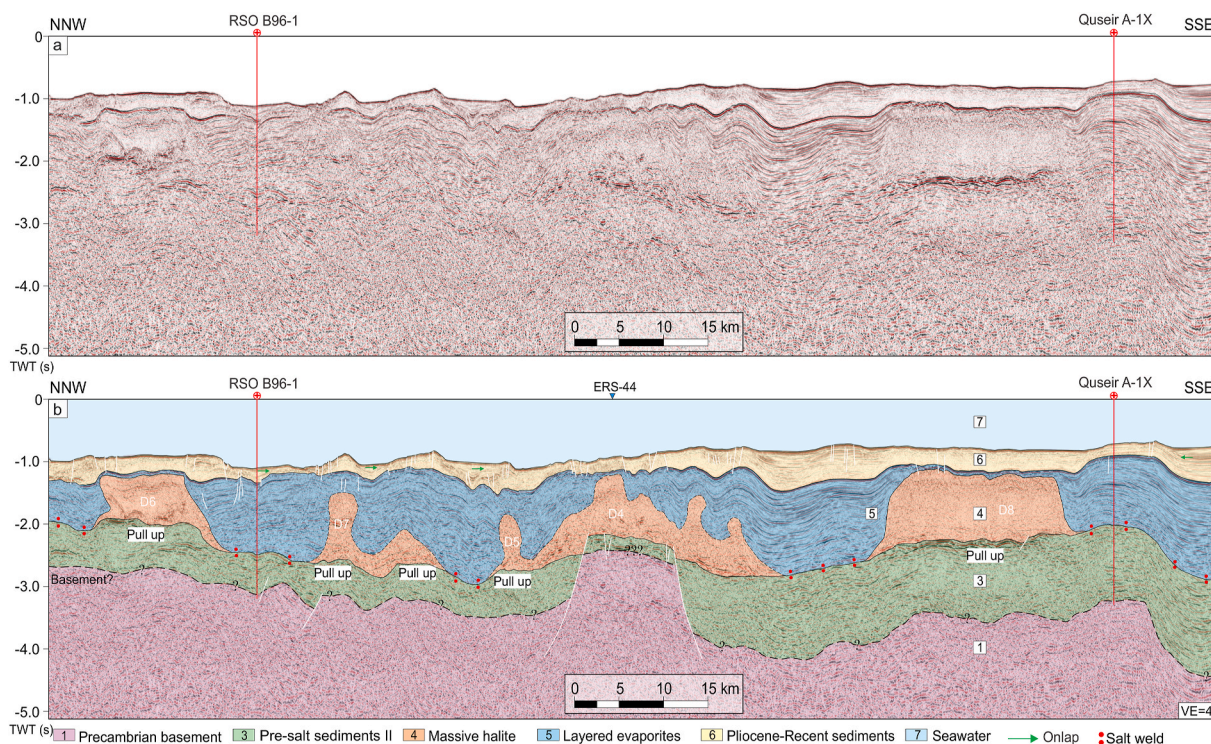
Fig. 13. (a) Uninterpreted and (b) Interpreted NNW-SSE seismic profile, displaying salt diapirs (D), extensional faults (white lines), and large thickness variations of each seismic sequence. Section location is shown in Fig. 3. VE: vertical exaggeration.

Table 1
The average velocity of the available units in the NRS (Gaulier et al., 1988; Makris and Rihm, 1991; Rihm et al., 1991; Saleh et al., 2006; Ligi et al., 2018).

Unit Name	Average Velocity (m/s)
Seawater	1525
Plio-Quaternary	2000
Layered evaporites	3300
Salt layer	4200
Pre-salt II	2700
Pre-salt I	2800
Basement	3500

trending NW-SE to NNW-SSE and NE-SW to ENE-WSW (Fig. 17). Most of the NW-SE to NNW-SSE normal faults dip seaward (NE to ENE) and their lengths along strike vary from 1 to 11 km. The NE-SW to ENE-WSW set mainly dips toward the SE, and their lengths along strike range between 1 and 7 km (Fig. 17).

The TWT maps of the top and base of the massive salt sequence are shown in Fig. 18a and b, respectively. The map of the salt-layer top shows that the minimum depths are distributed along the crests of the salt walls, ranging from 1.0 to 1.3 s TWT (~1000–1300 m). In contrast, the deepest areas are recorded in the subbasins formed between the salt structures and in the western and northwestern regions of the study area, parallel to the present shoreline (Fig. 18a). The depths in these regions vary between about 2.1 and 3.0 s TWT (~2450–3700 m bsl). The fault density sharply decreases toward the top of the salt unit, where only a few normal structures, trending NNE-SSW, NW-SE and E-W, were recognized in the eastern sector of the offshore Quseir. They are located around the volcanic edifice mentioned above and display lengths varying from 1.5 to 9 km (Fig. 18a). The minimum depths of the salt base (Fig. 18b) are found beneath the salt walls with values ranging from 1.6 to 2.1 s TWT (~2650–3800 m bsl), while the maximum depths are in the regions between the salt structures, which vary from 2.2 to 3.1 s TWT (~2650–3900 m bsl). The fault interpretation below the massive salt

sequence is challenging. However, several major normal faults, all striking NW-SE parallel to the salt walls and lengths varying between 10 and 15 km, have been recognized to offset the salt base. The subsalt normal faults dip NE and SW and define a few major highs (Fig. 18b).

Three isopach maps have been made for the Plio-Quaternary, layered evaporites and salt layer to analyze their thickness distribution (Fig. 19). The Plio-Quaternary sequence has a maximum thickness of over 1.2 s TWT (~1200 m), reached in the northwestern part of the offshore Quseir. This thickness decreases dramatically eastward and southeastward, in correspondence with the crests of the salt structures, with a TWT value from 0.1 to 0.2 s (~100–200 m). The thickness of the sediments increases in the regions between the salt structures with an average value of about 0.5 s TWT (~500 m; Fig. 19a). The isopach map of the layered evaporites shows the highest and abrupt thickness variations, approaching the minimum thickness in the areas directly above the salt walls and stock (0.1 s TWT; 175 m). The thickness of the layered evaporites increases dramatically in the subbasins located between the salt structures, where it ranges from 0.8 to 1.5 s TWT (1400–2600 m; Fig. 19b). The isopach map of the massive salt sequence exhibits an opposite trend as the maximum thicknesses are located at the salt walls, with values ranging from 0.6 to 1.2 s TWT (~1250–2500 m). The minimum values, ranging between 0 and 0.1 s TWT (~0–400 m), are found in the welded basins (Fig. 19c).

5. Discussion

5.1. Structural evolution

Based on the interpretation of seismic sections, a four-stage tectonostratigraphic model for the structural evolution of the southern part of offshore Quseir is proposed. The model begins with the deposition of the pre-salt sediments, followed by the precipitation of the salt layer. This model explores salt movement up to the present day (Fig. 20), emphasizes the distribution of salt formations (the salt layer and layered evaporites), and investigates the timing of salt movement, shifting of
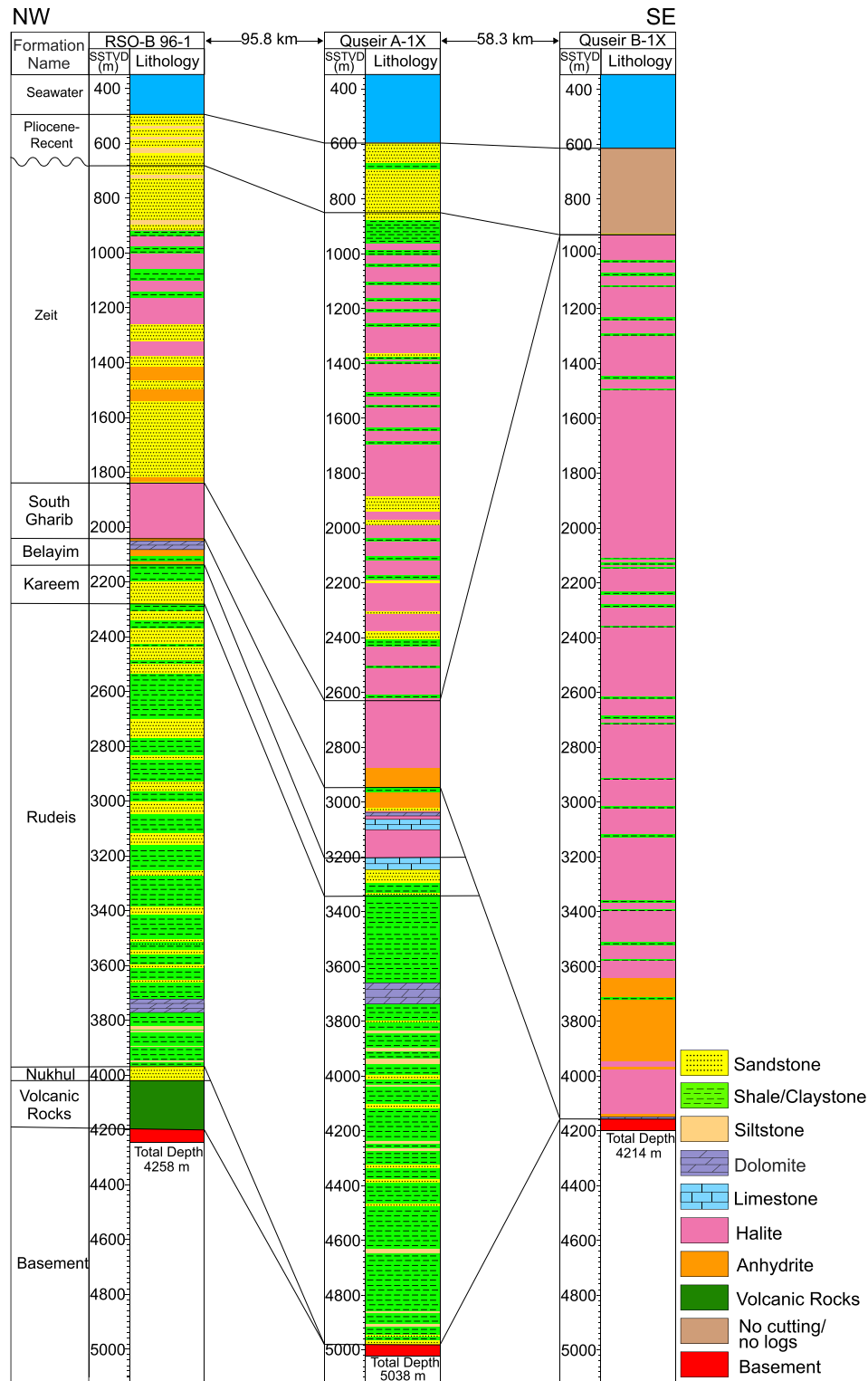
Fig. 14. Stratigraphic correlation of well RSO-B 96–1 (northwestern part to the offshore Quseir), well Quseir A-1X (southwestern part to the offshore Quseir), and well Quseir B-1X in the southeastern part of offshore Quseir. Wells location is shown in Fig. 3.

depocenters, and welding/salt depletion at specific locations.

5.1.1. Stage 1 (Middle-Late Miocene)

Before deposition of the Middle Miocene salt layer, a structural low bounded by two low-angle normal faults (F1 and F2) was present in the area. A Cretaceous-Eocene pre-rift and Late Oligocene-Middle Miocene syn-rift successions may have been present at the base of this basin,

although pre-rift strata were never confirmed by drilling data (Bosworth et al., 2020). Nevertheless, it must be stressed that wells were usually drilled on structural highs, where such successions were thin, not deposited, or eroded. These successions have been combined in one seismo-stratigraphic unit labelled pre-salt sequence (Fig. 20d). The pre-salt sequence overlies the crystalline basement unconformably and shows large lateral variations; its thickness decreases northeastward
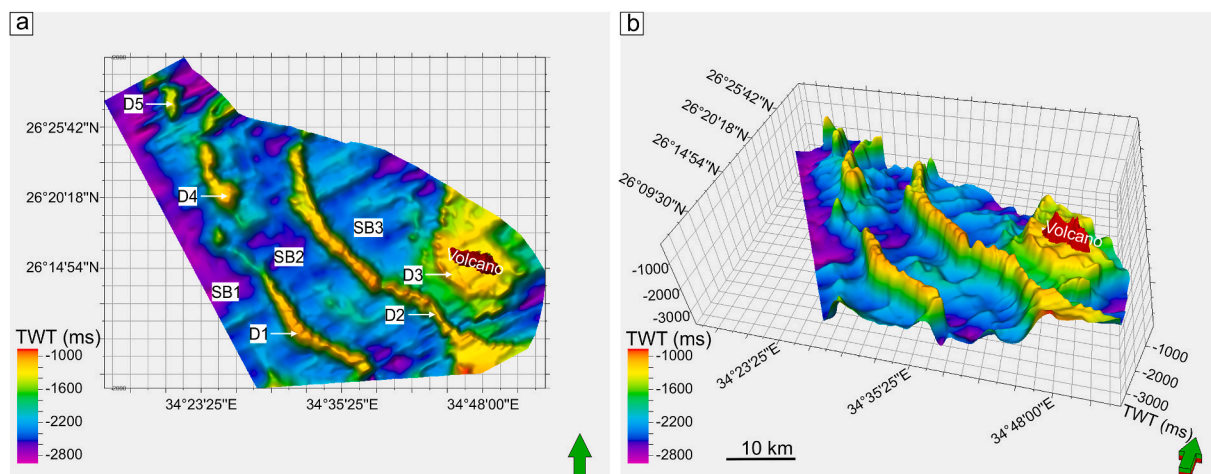
Fig. 15. Top (a) and 3D (b) views of the top of the salt layer displaying five salt walls trending NW-SE to NNW-SSE. D and SB denote diapir and subbasin, respectively. The movie is attached to the supplementary materials.

from about 2200 m in the depocenter to approximately 1300 m in the northeastern end of the graben (Fig. 20d). However, the main massive salt layer was precipitated in the Middle-Late Miocene during the hyperextension stage of the northern Red Sea and was restricted to the necking and distal domains, but is absent in the proximal domain (Ali et al., 2023, their Figs. 5 and 10). Estimating the initial thickness of the salt remains challenging due to the lack of seismic and well data, the base of salt layer may not be flat (i.e., initial salt is thicker in grabens and half grabens), and salt flows in and out of the study area. However, based on the interpreted seismic sections and forward modeling, a crude estimation is made of approximately 1500 m of mobile salt being precipitated in the deepest part of the basin (*see* Ali et al., 2023). Locally, in the southeastern part of the offshore Quseir, only a few hundred meters of salt was precipitated (Fig. 20d). Seawards, beyond these basement highs, the current thickness of the salt layer is ~1200 m. Although the lower salt layer is generally seismically transparent (Figs. 5–13), it includes few high-amplitude reflections. These reflections are probably related to non-evaporitic lithologies (e.g. carbonate interbeds) or to thin anhydrite layers dragged by salt flow, similar to what is observed within the salt structures (Figs. 5, 9 and 10). This interpretation is compatible with the available boreholes where the salt layer consists of halite intercalated with thin beds of anhydrite and with observations reported in the previous literature (Fig. 14; Izzeldin, 1987; Orszag-Sperber et al., 1998; Koyi, 2001; Mitchell et al., 2017). Some of the basement faults are assumed to be obscured by diapirs. However, several reactivated basement faults are observed in the seismic sections (Figs. 9–11), forming structural highs beneath the salt layer and the diapirs (Figs. 10 and 20d).

The precipitation of the salt layer was followed by the deposition of the layered evaporites in the Late Miocene (Figs. 4 and 14). Growth seismic sequences and moderate to large thickness variation are observed in these sediments, which indicate a Late Miocene synhalokinetic deposition (Figs. 12 and 20d). During this period, several NW-SE basement faults were active. They resulted in the formation of depressions where layered evaporites deposited, causing differential loading and withdrawal of the underlying salt (Fig. 20d). These observations indicate that the northern Red Sea underwent thick-skinned extension during the Middle Miocene. Movement along and reactivation of basement faults and subsequent and accompanying differential loading triggered salt movement (Koyi, 1991; Vendeville and Jackson, 1992a; 1992b; Koyi et al., 1993a; Jackson and Vendeville, 1994). Variations in the thickness of the layered evaporites and the structures displayed between the salt diapirs may indicate the passive stage of diapiric growth with the beginning of the deposition of the layered evaporites. The continuous movement of the major reactivated

basement faults and salt movement caused the formation of several suprasalt normal faults with NW to NNW dominant trend, parallel to sub-parallel to strike of the salt structures (Fig. 17b and 20d). The downlaps of the layered evaporite reflections near the present Egyptian shoreline are probably generated by hanging wall subsidence above a low-angle growth fault (Fa1, Fig. 12).

5.1.2. Stage 2 (Early Pliocene)

The Pliocene-Quaternary sequence is characterized by several sedimentary cycles (Figs. 10 and 12), which are divided into two main stages for simplicity. The Early Pliocene siliciclastic deposits were unconformably deposited above the layered evaporites, which were mobile (Fig. 14). The resulting erosional surface (labelled S-reflector) is sharp and evident at different locations in all the seismic sections (Figs. 5–13). Erosion of the layered evaporites, attributed to an abrupt fall of the Red Sea level in the latest Miocene or the earliest Pliocene (Mitchell et al., 2021), was probably due either to subaerial exposure (Colombo et al., 2014) or to the effect of waves in the shallow marine environment (Mitchell et al., 2017). The S-reflector is strongly reflective and continuous above the salt diapirs and anticlines of the layered evaporite sequence. In contrast, this erosive surface is vague in the basins, where Pliocene reflections seem to be conformable with those of layered evaporites. It is commonly regarded as a correlative conformity (Cartwright et al., 1993; Li and Schieber, 2022), indicative of depositional continuity (Figs. 5–13). This observation suggests that the top surface of the layered evaporites was probably not flat but displayed relief due to salt movement, and some parts of the surface remained submerged even during the drawdown of the Red Sea level.

The large thickness variation in the Pliocene sequence and its discordant relationship with the layered evaporites are interpreted to indicate that halokinesis was active during this period, creating minibasins flanked by salt diapirs (Fig. 20c). Several growth seismic sequences were observed within the mini-basins, onlapping the uplifted layered evaporites. Furthermore, toward the shoreline, indication of depocenters migration is evident, indicating salt basinward flow (Figs. 5–12). Preexisting suprasalt faults remained active while new ones were formed due to the continuous salt evacuation and probably due to continued movement along the basement faults. Movement along the subsalt and suprasalt faults and the differential loading in stages 1 and 2 were responsible for the evacuation and expulsion of most of the salt layer into the layered evaporites and the development of the major salt structures offshore Quseir. The basement highs northeast of the master faults within the basin (F2 and F3) may have hampered seaward salt flow (Figs. 5 and 20c).
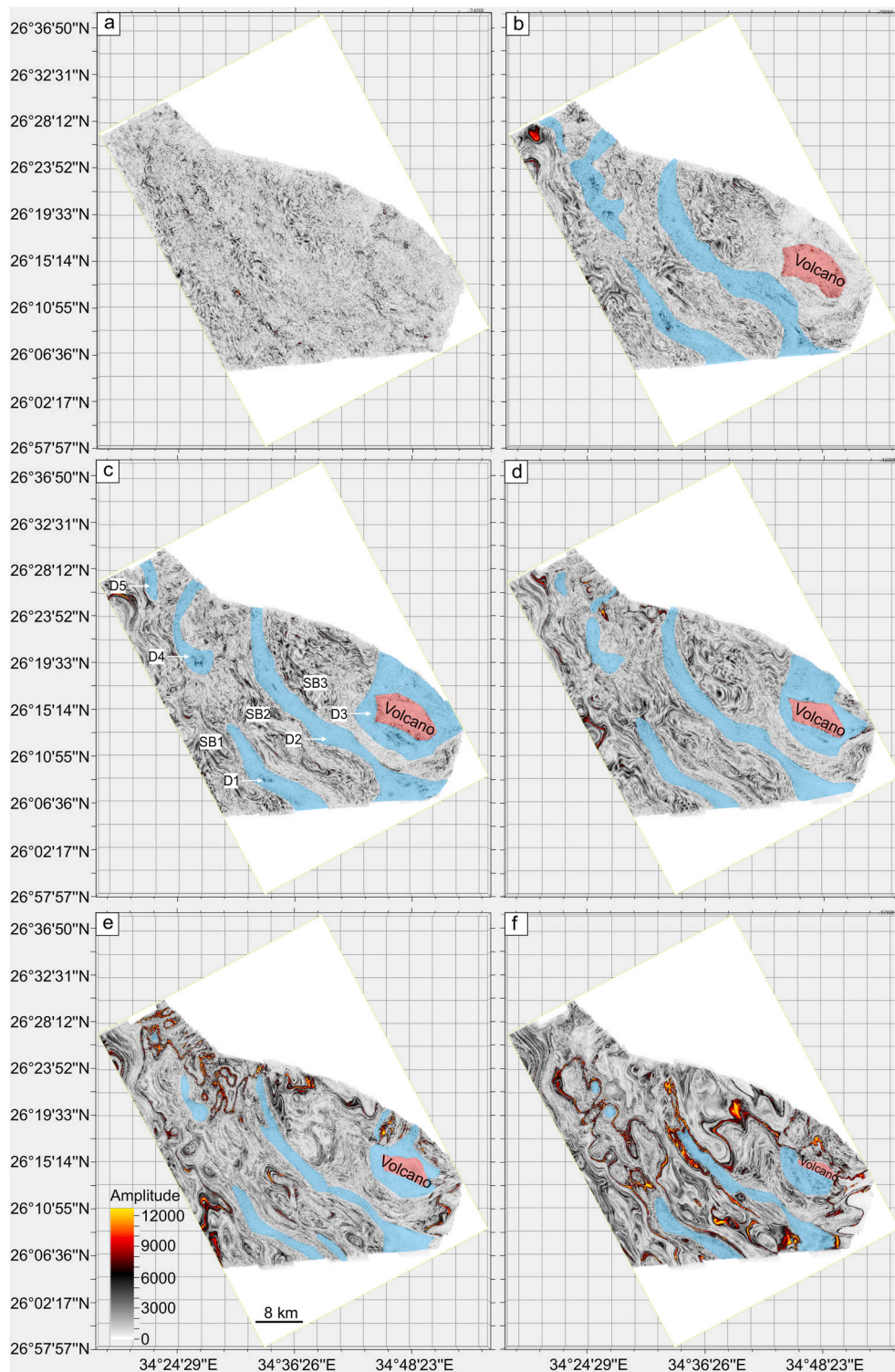
Fig. 16. Time slices at −2.5 (a), −2.0 (b), −1.8 (c), −1.6 (d), −1.4 (e), and −1.2 s (f) showing the distribution of salt walls in the offshore Quseir. Blue and red polygons denote the boundary of salt walls and seamount, respectively. D is diaper, and SB is subbasin. (For interpretation of the references to colour in this figure legend, the reader is referred to the Web version of this article.)

5.1.3. Stage 3 (Plio-Pleistocene)

Continuous evacuation of the remaining salt during the Plio-Pleistocene caused subsidence between the major salt structures. New siliciclastic sediments were deposited unconformably above the Early Pliocene sequence, indicating erosional surfaces between two sedimentary cycles (Figs. 2, 6, 8, 10 and 12b). Movement of the underlying salt caused the migration of depocenters southwestward. Furthermore,

during this stage, most of the remaining mobile salt in the southwestern region of the offshore Quseir was depleted (Figs. 5–11 and 20b). In contrast, a significant amount of salt, with an average thickness of 500 m, remained surrounding the basement highs in the southeastern sector of the study area (Fig. 20b). Most of the suprasalt faults die out before cutting the seafloor. However, in the northwestern and southeastern regions of the offshore Quseir, several suprasalt faults have been
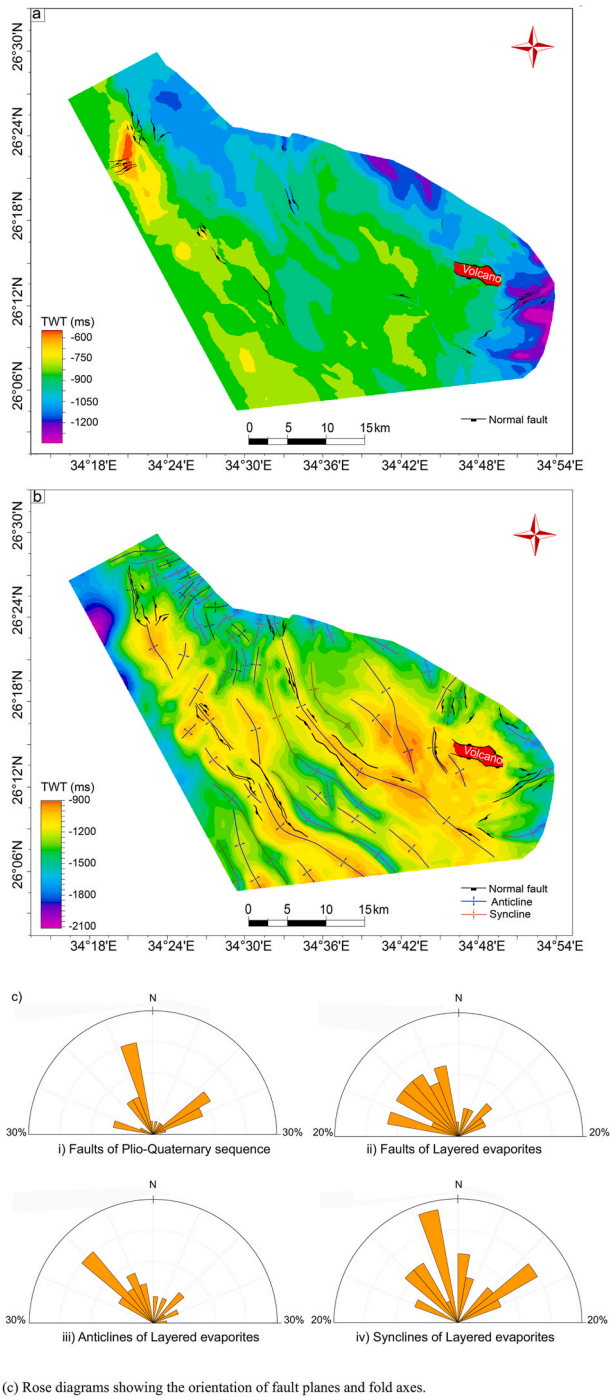
Fig. 17. TWT map of top (a) Plio-Quaternary sediments and (b) layered evaporites.

recognized offsetting the seafloor with throws ranging from a few tens of metres to 200 m (Figs. 1, 5 and 17a and 20b).

5.1.4. Stage 4 (Volcanic Eruption)

The Quaternary period witnessed a magmatic event in the northern Red Sea as several volcanic edifices have been recognized from geophysical data (Cochran et al., 1986; Ali et al., 2022a; 2022b). The two basement highs recognized in the southeastern region of the Quseir, near the Brothers Islands, were identified as volcanic sites (Ali et al., 2022a). The magmatic supply followed a generalized crustal thinning stage and probably erupted through major fault zones (F2 and F3). The Plio-Quaternary sequence shows significant thinning toward the salt
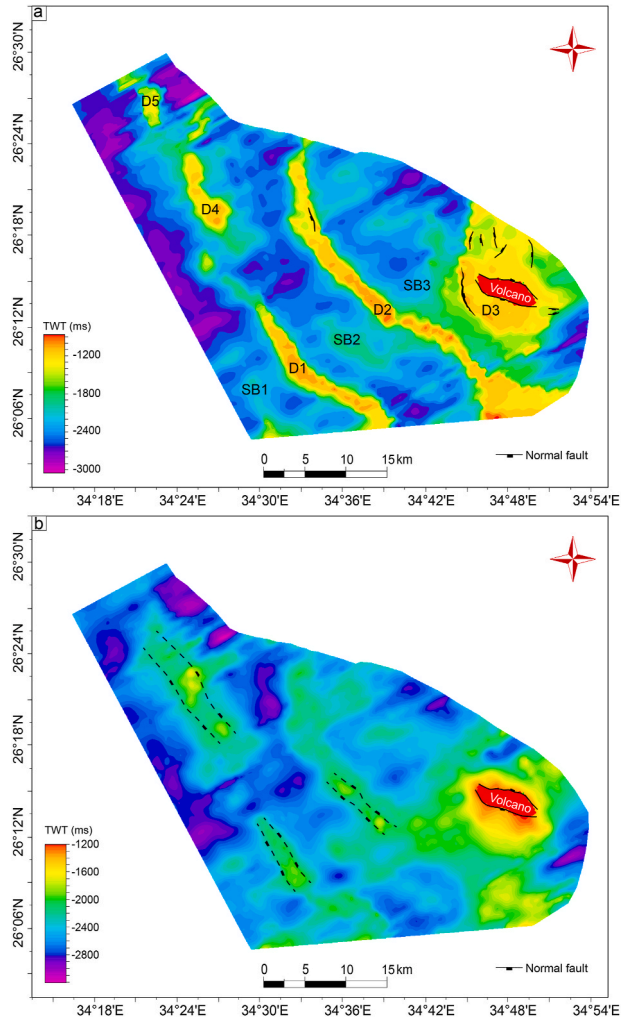

Fig. 18. TWT map of top salt (a) and base salt (b). D is diapir, and SB is subbasin.

diapirs in some segments of the study area, suggesting continued salt movement and growth of salt structures (Figs. 2, 5 and 20a). Moreover, most of the salt structures offshore Quseir experienced minor sag or diapiric falls related to the continuous extension in the Red Sea, which is still an active rift (e.g., Cochran and Martinez, 1988; Bosworth et al., 2005). The recorded seismicity in the northern Red Sea indicates a large number of earthquakes, which are characterized by low to moderate magnitudes (Al-Ahmadi et al., 2014; Bosworth et al., 2020). The number of seismic events and those of the larger earthquakes gradually increase northward, reaching their maximum at the Sinai triple junction (Bosworth et al., 2020, their Fig. 9.3). Based on the global Centroid Moment Tensor (CMT) catalogue, the focal mechanisms of the earthquakes, as expected, are predominantly normal dip-slip with strikes in the NNW-SSE and NW-SE directions, parallel to the rift orientation of the Red Sea (Badawy et al., 2008; Abdel-aal and Yagi, 2017).

5.2. Thick-skinned versus thin-skinned extension

Several key features have been observed in the seismic data to support thick-skinned extension as a dominant mechanism for salt mobilization offshore Quseir (Figs. 10 and 20). Thick-skinned extension accompanied by syn-kinematic sedimentation (which has caused differential loading) are likely to have triggered salt movement (Fig. 20). The seismic data used in this study do not provide any evidence to support a progradational loading system or the existence of a
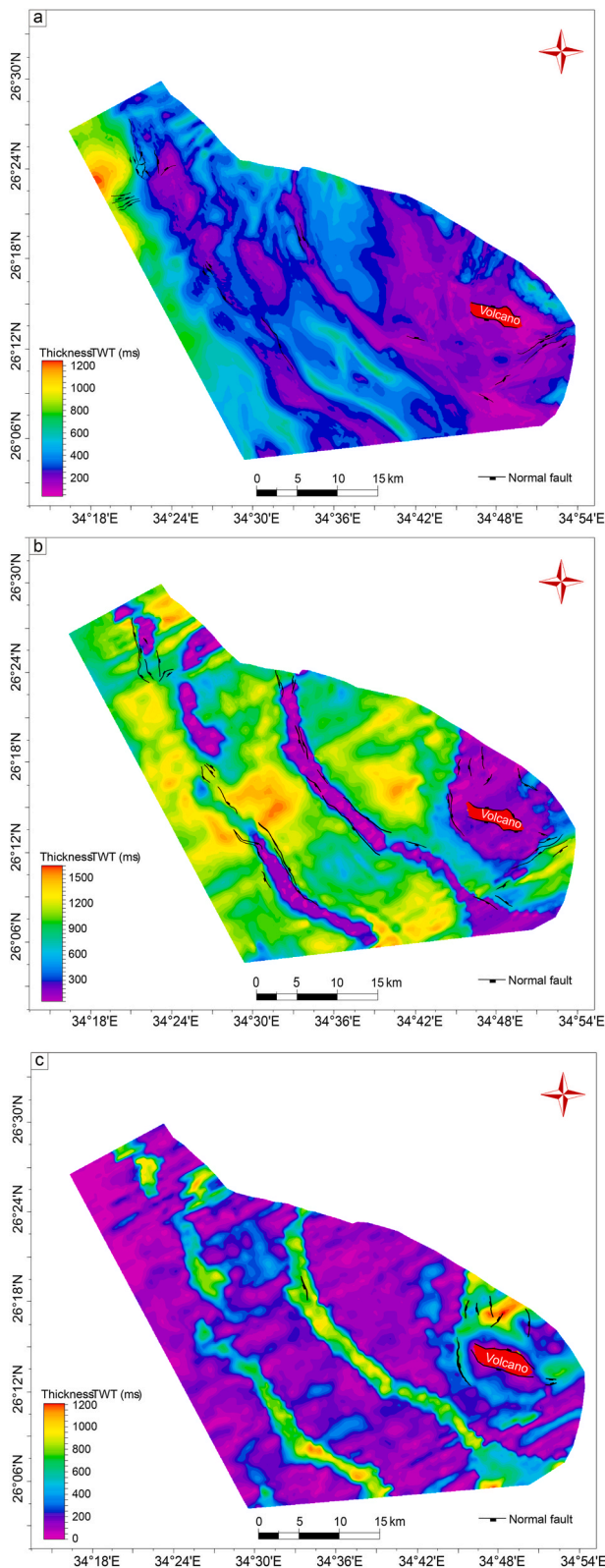
Fig. 19. Isopach maps of (a) Plio-Quaternary sequence, (b) layered evaporites, and (c) salt layer.

sedimentary wedge. The following arguments are used to support the thick-skinned extension.

1. Existence of reactivated basement normal faults. Several subsalt faults were recognized on the seismic sections. These faults penetrated the base of the salt sequence and are interpreted to have caused asymmetric sedimentation and differential loading on the underlying salt layer (Figs. 9–11 and 20).

2. Large thickness variations in the layered evaporites and Plio-Quaternary deposits (across basement faults). This thickness variation could be related to displacements of basement faults or/and salt withdrawal. The maximum thickness of the overburden is found directly above the hanging wall of the subsalt faults (e.g. Figs. 5 and 9).

3. Significant topography at the base of the salt sequence. The seismic sections display large changes in the topography of the base salt, especially across the major subsalt faults (F1 and F2; Figs. 5, 10 and 12). Subsalt topography, likely generated by movement along basement (subsalt) faults, played an important role in triggering salt movement and probably controlled the spatial distribution of salt structures.

4. Trend of salt walls. Several salt walls are parallel to and grow above the main structural/fault trend of the Red Sea (NW-SE) (Figs. 10 and 18).

5. The existence of gravity gliding and suprasalt faults. Subsalt faults contributed to a change in the slope of the northern Red Sea margin dipping towards the ENE. This has caused extension and gliding of the overburden basinwards above the salt, resulting in the formation of many suprasalt faults. Most of these faults trend NW-SE and are located above and close to the diapir crests (Figs. 5–13).

6. Diapir fall or sag. Suprasalt faults were observed above the crests of the salt structures, indicating continued extension of the area and diapiric fall. It is assumed that the feeding salt layer is depleted and welds formed below mini-basins (e.g. Fig. 5).

Seismic observations indicate that most of the basement faults in the central part of offshore Quseir die out within the salt layer or cannot be traced in the cover units, indicating a decoupled system (e.g. Figs. 6 and 7). However, some major subsalt faults penetrated the salt layer and the overburden, suggesting a coupled system in the eastern and western sectors of the offshore Quseir (Figs. 5, 10 and 11). It is generally thought that the basement will be stretched and faulted in a rifted margin that has undergone crustal extension. Such deformation will directly affect any salt layer resting on this basement. This is corroborated by several physical experiments (Koyi et al., 1993a; 1993b; Withjack and Callaway, 2000; Dooley et al., 2004; 2017; Burliga et al., 2012; Dooley and Hudec, 2017). The salt layer in the Red Sea was precipitated above a faulted basement, which strongly impacted salt flow and sediment deposition. Therefore, it is both likely and expected that salt mobilization was within the framework of thick-skinned tectonics. Salt movement began with the precipitation of the layered evaporites during Late Miocene and continued until Pleistocene, creating several salt walls in the NW-SE to NNW-SSE directions. Although, the interpreted salt structures do not reach the seafloor, their growth must have continued after the deposition of the S-reflector, which is bent above the salt diapirs. The massive salt layer was probably depleted, or the extension rate was greater than the salt supply to the diapirs during the Pleistocene, as several local sag basins and grabens have been recognized above the salt diapirs. They were probably generated due to the salt fall during continued extension along the margin (Figs. 5–11). The seafloor of the study area is irregular, showing changes in bathymetry, indicating that these areas are currently tectonically (and probably, halokinetically) active. Salt movement ceased in some parts of the central region of the Red Sea earlier at the Miocene-Pliocene boundary, implying that salt expulsion was heterogeneous (Mitchell et al., 2022).

Rowan (2014) and Tubbs et al. (2014) suggested that the Middle-Late Miocene salt layer was dominantly deformed by thin-skinned gravitational failure, while Smith and Santamarina (2022) proposed that carbonate platforms and alluvial sediment fans drive salt withdrawal. Based on the observations above, we think that thick-skinned extension strongly contributed to salt mobilization and
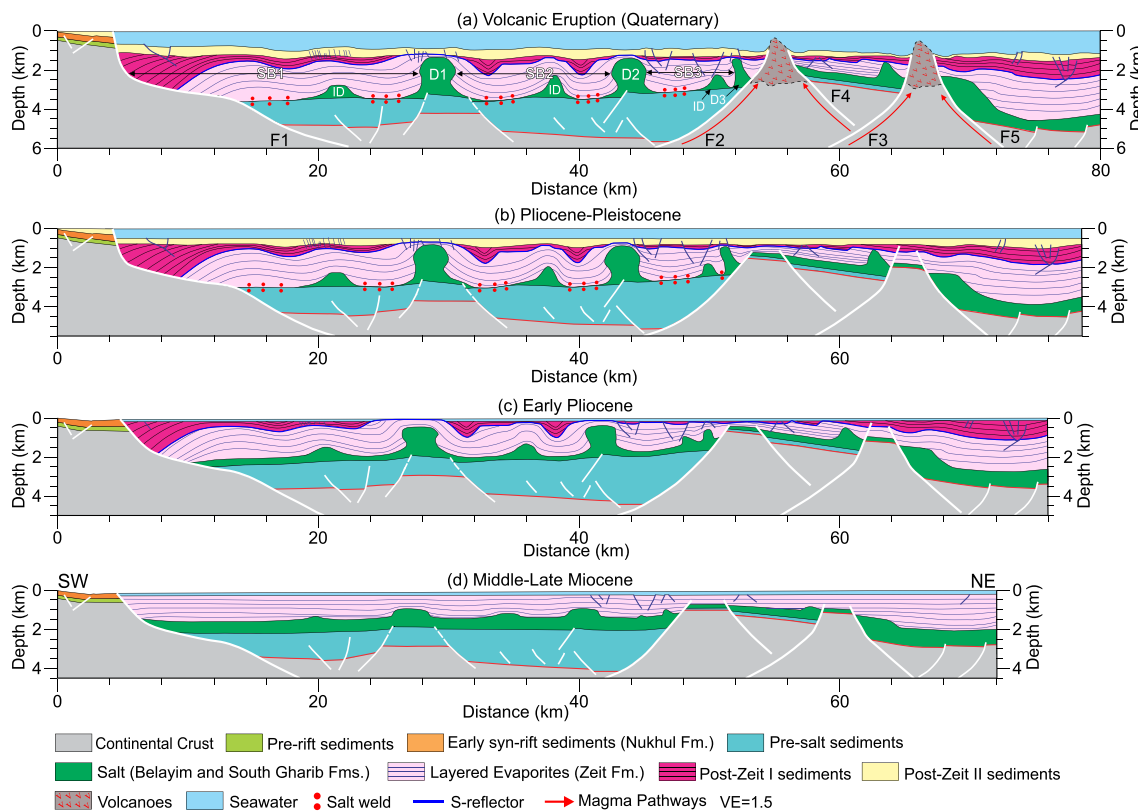
Fig. 20. Schematic reconstruction of the southern part of the offshore Quseir from the Middle Miocene to the present.

continued movement in the northern Red Sea. However, the presence of gravity gliding, suprasalt faults, ramp syncline basins, and diapir sag show that the thick-skinned extension induced thin-skinned extension offshore Quseir. The thin-skinned extension in offshore Quseir is not considered to be regional; the main basement faults compartmentalize the area into sub-basins where thin-skinned extension occurs locally (Fig. 10). In addition, although there is lateral movement of the layered evaporites and Plio-Quaternary sequence, some of the diapirs remain "resting" above basement horsts influenced by two main basement faults on both sides of the diapirs. Figs. 9 and 10 display a good example of salt wall D4, formed above a horst where salt has moved up-dip to the low-pressure zones in the footwall of the subsalt faults. In other words, diapirs feed from both sides of the horst and stay above the basement faults. In an extensional tectonic system where basement faults dominate, it is likely that the movement of these faults does influence salt diapirism, both as triggers and/or affects the continued evolution of salt structures. Furthermore, it is thick-skinned extension does not exclude thin-skinned extension happening locally in areas between the major basement faults.

5.3. Comparison with physical models

Several examples for salt structures triggered by basement faults are reported by Ford and Vergés (2021) in the Pyrenees margin, in the Danish Basin (e.g. Koyi and Petersen, 1993; Hansen et al., 2021) and the Nordkapp Basin in the Barents Sea (e.g. Koyi et al., 1993b; Rojo et al., 2019). Many studies have described the impact of the basement faults on salt mobilization by using scaled analogue models (e.g. Koyi and Petersen, 1993; Koyi et al., 1993a; Nilsen et al., 1995; Rojo et al., 2020). Seismic observations in the study area are consistent with the results from physical models by Koyi and Petersen (1993; their Fig. 5) and Koyi et al. (1993a; their Figs. 5 and 6) simulating the effect of basement faults on diapirs. The results from these analogue models can be used to suggest that the basement faults in the northern Red Sea strongly influence

the movement of the Middle-Late Miocene salt layer and trigger the growth of salt structures. Most of the interpreted seismic sections indicate that basement faults formed half-grabens overlain by thick overburden units, causing differential loading on the salt layer. The salt moved up-dip to the low-pressure zones in the footwall and up-dip along the uplifted part of the rotated hanging walls (e.g. Figs. 5 and 11). The seismic interpretation suggests that most of the salt walls in offshore Quseir are associated with basement-involved faults (Figs. 5–13). Sandbox model results by Koyi et al. (1993a; their Fig. 6) display that salt structures triggered by subsalt faults are not necessarily located directly above these faults. Based on the results from physical models by Withjack et al. (1990), Koyi et al. (1993a) and others, the location of the resulting salt structures is strongly associated with the overburden deformation due to the basement-involved faulting. They suggested that the basement faults stretched the overburden and created the space through which the salt layer could flow up-dip. Our seismic observations are strongly consistent with this suggestion, as all the salt diapirs offshore Quseir are found below weak zones of the layered evaporites and the Plio-Quaternary sequence. This is also the case for salt wall D3, which is not associated with basement faults (Figs. 5 and 6).

In the southeastern part of the offshore Quseir, a few pillows have been recognized on the uplifted sector of the rotated hanging walls of basement faults. These pillows are immature and smaller compared to the major salt diapirs (D1-D5), located directly above the tip of the basement faults. These observations are compatible with the results of a physical model by Koyi et al. (1993a; their Model 3, Fig. 5b). They suggested that, along the fault, salt flows faster due to the higher loading. However, part of the salt in the half-graben is displaced along the tilted hanging wall, where it may form a pillow or an immature salt structure (Figs. 5 and 6).

Furthermore, the seismic data show several ramp-syncline basins (RSBs) characterized by asymmetric and landward depocenter migration. The kinematics and stratigraphic architecture of these structures have been documented in both analogue models (McClay and Scott,

1991; McClay, 1996; Dooley et al., 2017; M. Pichel et al., 2019) and numerical models (Pichel et al., 2018). Model results show two types of RSBs: extensional/classic and salt-detached RSBs. We have used model results to identify extensional and salt-detached RSBs offshore Quseir. The classic RSBs are found on the hanging wall of the F1 master fault (Figs. 10 and 12) and display asymmetric depocentres with basinward-dipping axial trace. However, the geometry and the axial trace of the observed extensional RSBs are strongly compatible with the modeled RSBs by McClay (1996), some components are probably salt-related (Fig. 10). The salt-detached RSBs were recognized in the SB2 and SB3 between the major salt structures (i.e., between D4 and D2 salt diapirs; Figs. 9 and 10), their geometry and axial trace are similar to the modeled salt-detached RSBs by Pichel et al. (2018). The Plio-Quaternary unit translates above the Middle-Late Miocene evaporite sequence. Like the extensional RSBs, the salt-detached RSBs show a basinward-dipping axial trace with landward-shifting depocenters displaying extension-related components (Figs. 9 and 10). The surface boundaries of both RSBs are diachronous, and they have onlap, baselap and toplap terminations. The RSBs have been documented by Rowan (2014) above the hanging wall of basement faults in the Saudi Arabian margin.

6. Conclusions

Interpretation of two-dimensional and three-dimensional seismic surveys and borehole data support the presence of five major salt walls (D1-D5) and several immature salt structures in the central part of the Egyptian Red Sea rifted margin. The salt walls trend from NW-SE to NNE-SSW and have been interpreted to be associated with basement faults. They show relatively irregular crests and moderately-dipping flanks with an average width of 5 km at the base and 1.5 km at their crest. Salt structures exhibit variable amplitudes between 0.6 and 1.2 s TWT (~1250–2500 m). Salt wall D2 is the longest salt structure, with a total length of approximately 46 km. Salt structures are associated with overburden faults and folds. Our observations support a decoupled system in the offshore Quseir. However, in the eastern and western parts of the study area, the existence of major subsalt faults penetrating the overburden suggests that the stretching overburden was coupled to the subsalt strata and basement.

This study demonstrates that thick-skinned extension was the main driver for salt mobilization in the offshore Quseir. However, locally, the thick-skinned extension resulted in minor thin-skinned extension, where subsalt deformation is decoupled from that in the overburden. Growth seismic sequences, large thickness variations, and diapiric contacts are observed in the layered evaporites, suggesting that the study area underwent thick-skinned extension during the Late Miocene, i.e., extension affected the continental crust. Furthermore, the presence of suprasalt faults, SW-shifting depocenters, and thickness variation in the Plio-Quaternary sediments indicate that thick-skinned extension continues in offshore Quseir. Moreover, in the central part of the northern Red Sea, the massive salt layer was probably depleted during the Quaternary and the salt walls experienced diapiric fall due to the continuous extension. A comparison between seismic observations and the results from several physical models investigating the influence of basement faulting on salt mobilization supports our interpretation that the basement faults offshore Quseir had a significant impact on the movement of the salt layer and triggered the growth of salt structures.

Author statement

Conceptualization: Moamen Ali, Hemin Koyi, Alessandro Decarlis.
Data curation: Moamen Ali, William Bosworth.
Investigation: Hemin Koyi, Alessandro Decarlis.
Methodology: Moamen Ali, Hemin Koyi.
Project Administration: Alessandro Decarlis, Hemin Koyi.
Resources: Marco Ligi, William Bosworth, Alessandro Decarlis.
Software: Moamen Ali.

Supervision: Alessandro Decarlis, Hemin Koyi, William Bosworth, Philip Ball, Marco Ligi.
Visualization: Moamen Ali, Alessandro Decarlis, William Bosworth, Marco Ligi.
Writing – original draft: Moamen Ali.
Writing – review & editing: Hemin Koyi, Alessandro Decarlis, William Bosworth, Marco Ligi, Philip Ball.

Data availability

The authors do not have permission to share data.

Appendix A. Supplementary data

Supplementary data related to this article can be found at https://doi.org/10.1016/j.jsg.2023.104955.

References

Abdel-aal, A.K., Yagi, Y., 2017. Earthquake source characterization, moment tensor solutions, and stress field of small-moderate earthquakes occurred in the northern Red Sea Triple Junction. Geosci. J. 21, 235–251.

Al-Ahmadi, K., Al-Amri, A., See, L., 2014. A spatial statistical analysis of the occurrence of earthquakes along the Red Sea floor spreading: clusters of seismicity. Arabian J. Geosci. 7, 2893–2904.

Ali, M., Darwish, M., Essa, M.A., Abdelhady, A., 2018. 2D seismic interpretation and characterization of the Hauterivian–Early Barremian source rock in Al Baraka oil field, Komombo Basin, Upper Egypt. J. Afr. Earth Sci. 139, 113–119.

Ali, M., Abdelhady, A., Abdelmaksoud, A., Darwish, M., Essa, M.A., 2020. 3D static modeling and petrographic aspects of the albian/cenomanian reservoir, komombo basin, upper Egypt. Nat. Resour. Res. 29, 1259–1281.

Ali, M., Ligi, M., Ceriani, A., Bouchaala, F., Bosworth, W., Decarlis, A., 2022a. Geophysical evidence for magmatism southwest of the Brothers Islands, northern Red Sea (offshore Quseir, Egypt). Tectonics 41, e2022TC007228.

Ali, M., Ligi, M., Ceriani, A., Bouchaala, F., Bosworth, W., Decarlis, A., 2022b. Birth of a large quaternary volcanic edifice southwest of the Brothers islets, northern Red Sea, Egyptian margin. In: Working Group on Mediterranean Ophiolites Conference, vol. 1. Ofioliti, Italy. Abstracts.

Ali, M., Decarlis, A., Ligi, M., Ball, P., Bosworth, W., Ceriani, A., 2023. Red Sea rifting in central Egypt: constraints from the offshore Quseir province. J. Geol. Soc. 180 https://doi.org/10.1144/jgs2022-105 jgs2022-j2105.

Almalki, K.A., Ailleres, L., Betts, P.G., Bantan, R.A., 2015a. Evidence for and relationship between recent distributed extension and halokinesis in the Farasan Islands, southern Red Sea, Saudi Arabia. Arabian J. Geosci. 8, 8753–8766.

Almalki, K.A., Betts, P.G., Ailleres, L., 2015b. The Red Sea–50 years of geological and geophysical research. Earth Sci. Rev. 147, 109–140.

Alsharhan, A.S., Salah, M.G., 1997. A common source rock for Egyptian and Saudi hydrocarbons in the Red Sea. AAPG (Am. Assoc. Pet. Geol.) Bull. 81, 1640–1659.

ArRajehi, A., McClusky, S., Reilinger, R., Daoud, M., Alchalbi, A., Ergintav, S., Gomez, F., Sholan, J., Bou-Rabee, F., Ogubazghi, G., 2010. Geodetic constraints on present-day motion of the Arabian plate: implications for Red Sea and gulf of aden rifting. Tectonics 29.

Augustin, N., Van der Zwan, F.M., Devey, C.W., Brandsdóttir, B., 2021. 13 million years of seafloor spreading throughout the Red Sea basin. Nat. Commun. 12, 1–10.

Badawy, A., Mohamed, A.M.S., Abu-Ali, N., 2008. Seismological and GPS constraints on Sinai sub-plate motion along the Suez rift. Studia Geophys. Geod. 52, 397.

Ball, P.J., Stockli, D.F., Robbins, S., Tugend, J., Masini, E., 2018. Northern Red Sea: Unravelling the Tectono-Thermal Evolution of a Hyper-Extended Rift System. La Réunion Des Sciences de La Terre. Abstract 245.

Barakat, H., Miller, P., 1984. Geology and petroleum exploration, Safaga concession, northern Red Sea, Egypt. Egyptian General Petroleum Corporation, Cairo, pp. 191–214.

Beydoun, Z.R., 1989. The hydrocarbon prospects of the Red Sea-gulf of aden: a review. J. Petrol. Geol. 12, 125–144.

Beydoun, Z.R., Sikander, A.H., 1992. The Red Sea—gulf of aden: re-assessment of hydrocarbon potential. Mar. Petrol. Geol. 9, 474–485.

Bonatti, E., 1985. Punctiform initiation of seafloor spreading in the Red Sea during transition from a continental to an oceanic rift. Nature 316, 33–37.

Bonatti, E., Colantoni, P., Dellavedova, B., Taviani, M., 1984. Geology of the red-sea transitional region (22-degrees-n-25-degrees-n). Oceanol. Acta 7, 385–398.

Bosworth, W., 2015. Geological Evolution of the Red Sea: Historical Background, Review, and Synthesis. The Red Sea. Springer, pp. 45–78.

Bosworth, W., Sultan, M., Stern, R.J., Arvidson, R.E., Shore, P., Becker, R., 1993. Nature of the Red Sea crust: a controversy revisited: comment and reply. Geology 21, 574–576.

Bosworth, W., Crevello, P., Winn, R.D., Steinmetz, J., 1998. Structure, Sedimentation, and Basin Dynamics during Rifting of the Gulf of Suez and North-Western Red Sea. Sedimentation and Tectonics in Rift Basins Red Sea:-Gulf of Aden. Springer, pp. 77–96.

Bosworth, W., Huchon, P., McClay, K., 2005. The red sea and gulf of aden basins. J. Afr. Earth Sci. 43, 334–378.

Bosworth, W., Montagna, P., Pons-Branchu, E., Rasul, N., Taviani, M., 2017. Seismic hazards implications of uplifted Pleistocene coral terraces in the Gulf of Aqaba. Sci. Rep. 7, 1–13.

Bosworth, W., Khalil, S.M., Ligi, M., Stockli, D.F., McClay, K.R., 2020. Geology of Egypt: the Northern Red Sea. The Geology of Egypt. Springer, pp. 343–374.

Burke, K., Dewey, J.F., 1973. Plume-generated triple junctions: key indicators in applying plate tectonics to old rocks. J. Geol. 81, 406–433.

Burliga, S., Koyi, H.A., Chemia, Z., 2012. Analogue and numerical modelling of salt supply to a diapiric structure rising above an active basement fault. Geological Society, London, Special Publications 363, 395–408.

Cartwright, J.A., Haddock, R.C., Pinheiro, L.M., 1993. The lateral extent of sequence boundaries. Geological Society, London, Special Publications 71, 15–34.

Cochran, J.R., 1983. A model for development of Red Sea. AAPG Bull. 67, 41–69.

Cochran, J.R., 2005. Northern Red Sea: nucleation of an oceanic spreading center within a continental rift. G-cubed 6.

Cochran, J.R., Martinez, F., 1988. Evidence from the northern Red Sea on the transition from continental to oceanic rifting. Tectonophysics 153, 25–53.

Cochran, J.R., Martinez, F., Steckler, M.S., Hobart, M.A., 1986. Conrad Deep: a new northern Red Sea deep: origin and implications for continental rifting. Earth Planet Sci. Lett. 78, 18–32.

Colombo, D., McNeice, G., Raterman, N., Zinger, M., Rovetta, D., Sandoval Curiel, E., 2014. Exploration beyond seismic: the role of electromagnetics and gravity gradiometry in deep water subsalt plays of the Red Sea. Interpretation 2. SH33–SH53.

Dooley, T.P., Hudec, M.R., 2017. The effects of base-salt relief on salt flow and suprasalt deformation patterns—Part 2: application to the eastern Gulf of Mexico. Interpretation 5. SD25–SD38.

Dooley, T.P., Ken, M., Mark, H., Dirk, S., 2004. Basement Controls on Salt Tectonics: Results from Analog Modeling.

Dooley, T.P., Hudec, M.R., Carruthers, D., Jackson, M.P.A., Luo, G., 2017. The effects of base-salt relief on salt flow and suprasalt deformation patterns—Part 1: flow across simple steps in the base of salt. Interpretation 5. SD1–SD23.

El Khrepy, S., Koulakov, I., Gerya, T., Al-Arifi, N., Alajmi, M.S., Qadrouh, A.N., 2021. Transition from continental rifting to oceanic spreading in the northern Red Sea area. Sci. Rep. 11, 1–7.

Feldens, P., Mitchell, N.C., 2015. Salt Flows in the Central Red Sea. The Red Sea. Springer, pp. 205–218.

Fiduk, J.C., Rowan, M.G., 2012. Analysis of Folding and Deformation within Layered Evaporites in Blocks BM-S-8 &-9, Santos Basin, Brazil, vol. 363. Geological Society, London, Special Publications, pp. 471–487.

Ford, M., Vergés, J., 2021. Evolution of a salt-rich transtensional rifted margin, eastern North Pyrenees, France. J. Geol. Soc. 178, jgs2019–j2157.

Gaulier, J.M., Le Pichon, X., Lyberis, N., Avedik, F., Geli, L., Moretti, I., Deschamps, A., Hafez, S., 1988. Seismic study of the crust of the northern Red Sea and gulf of Suez. Tectonophysics 153, 55–88.

Girdler, R.W., Underwood, M., 1985. The evolution of early oceanic lithosphere in the southern Red Sea. Tectonophysics 116, 95–108.

Girdler, R.W., Whitmarsh, R., 1974. Miocene Evaporites in Red Sea Cores, Their Relavance to the Problem of the Width and Age of Oceanic Crust beneath the Red Sea.

Gordon, G., Hansen, B., Scott, J., Hirst, C., Graham, R., Grow, T., Spedding, A., Fairhead, S., Fullarton, L., Griffin, D., 2010. The Hydrocarbon Prospectivity of the Egyptian North Red Sea Basin. Geological Society, London, Petroleum Geology Conference Series. Geological Society of London, pp. 783–789.

Griffin, D.L., 1999. The late Miocene climate of northeastern Africa: unravelling the signals in the sedimentary succession. J. Geol. Soc. 156, 817–826.

Griffin, D.L., 2002. Aridity and humidity: two aspects of the late Miocene climate of North Africa and the Mediterranean. Palaeogeogr. Palaeoclimatol. Palaeoecol. 182, 65–91.

Hansen, T.H., Clausen, O.R., Andresen, K.J., 2021. Thick-and thin-skinned basin inversion in the Danish Central Graben, North Sea–the role of deep evaporites and basement kinematics. Solid Earth 12, 1719–1747.

Haq, B.U., Schutter, S.R., 2008. A chronology of Paleozoic sea-level changes. Science 322, 64–68.

Heaton, R.C., Jackson, M.P.A., Bamahmoud, M., Nani, A.S.O., 1995. Superposed Neogene Extension, Contraction, and Salt Canopy Emplacement in the Yemeni Red Sea.

Hempton, M.R., 1987. Constraints on Arabian plate motion and extensional history of the Red Sea. Tectonics 6, 687–705.

Hovland, M., Rueslåtten, H., Johnsen, H.K., 2015. Red Sea Salt Formations—A Result of Hydrothermal Processes. The Red Sea. Springer, pp. 187–203.

Hughes, G.W., Beydoun, Z.R., 1992. The Red Sea—gulf of aden: biostratigraphy, lithostratigraphy and palaeoenvironments. J. Petrol. Geol. 15, 135–156.

Hughes, G.W. ap G., Johnson, R.S., 2005. Lithostratigraphy of the Red Sea region. GeoArabia 10, 49–126.

Izzeldin, A.Y., 1987. Seismic, gravity and magnetic surveys in the central part of the Red Sea: their interpretation and implications for the structure and evolution of the Red Sea. Tectonophysics 143, 269–306.

Jackson, M.P.A., Vendeville, B.C., 1994. Regional extension as a geologic trigger for diapirism. Geol. Soc. Am. Bull. 106, 57–73.

Jackson, C.A.-L., Jackson, M.P.A., Hudec, M.R., Rodriguez, C.R., 2015. Enigmatic structures within salt walls of the Santos Basin—Part 1: geometry and kinematics from 3D seismic reflection and well data. J. Struct. Geol. 75, 135–162.

Jarrige, J., Ott d'Estevou, P., Burollet, P.F., Montenat, C., Prat, P., Richert, J., Thiriet, J., 1990. The multistage tectonic evolution of the Gulf of Suez and northern Red Sea continental rift from field observations. Tectonics 9, 441–465.

Khalil, S.M., McClay, K.R., 2001. Tectonic evolution of the NW Red Sea-gulf of Suez rift system. Geological Society, London, Special Publications 187, 453–473.

Khalil, S.M., McClay, K.R., 2002. Extensional fault-related folding, northwestern Red Sea, Egypt. J. Struct. Geol. 24, 743–762.

Khalil, S.M., McClay, K.R., 2009. Structural control on syn-rift sedimentation, northwestern Red Sea margin, Egypt. Mar. Petrol. Geol. 26, 1018–1034.

Koyi, H., 1991. Gravity overturns, extension, and basement fault activation. J. Petrol. Geol. 14, 117–142.

Koyi, H.A., 2001. Modeling the influence of sinking anhydrite blocks on salt diapirs targeted for hazardous waste disposal. Geology 29, 387–390.

Koyi, H., Petersen, K., 1993. Influence of basement faults on the development of salt structures in the Danish Basin. Mar. Petrol. Geol. 10, 82–94.

Koyi, H., Jenyon, M.K., Petersen, K., 1993a. The effect of basement faulting on diapirism. J. Petrol. Geol. 16, 285–312.

Koyi, H., Talbot, C.J., Tørudbakken, B.O., 1993b. Salt diapirs of the southwest Nordkapp Basin: analogue modelling. Tectonophysics 228, 167–187.

Le Magoarou, C., Hirsch, K., Fleury, C., Martin, R., Ramirez-Bernal, J., Ball, P., 2021. Integration of gravity, magnetic, and seismic data for subsalt modeling in the Northern Red Sea. Interpretation 9, T507–T521.

Li, Z., Schieber, J., 2022. Correlative conformity or subtle unconformity? The distal expression of a sequence boundary in the upper cretaceous mancos shale, henry mountains region, Utah, USA. J. Sediment. Res. 92, 635–657.

Ligi, M., Bonatti, E., Bortoluzzi, G., Cipriani, A., Cocchi, L., Caratori Tontini, F., Carminati, E., Ottolini, L., Schettino, A., 2012. Birth of an ocean in the Red Sea: initial pangs. G-cubed 13.

Ligi, M., Bonatti, E., Bosworth, W., Cai, Y., Cipriani, A., Palmiotto, C., Ronca, S., Seyler, M., 2018. Birth of an ocean in the Red Sea: oceanic-type basaltic melt intrusions precede continental rupture. Gondwana Res. 54, 150–160.

Lyberis, N., 1988. Tectonic evolution of the gulf of Suez and the gulf of Aqaba. Tectonophysics 153, 209–220.

Mahmoud, S., Reilinger, R., McClusky, S., Vernant, P., Tealeb, A., 2005. GPS evidence for northward motion of the Sinai Block: implications for E. Mediterranean tectonics. Earth Planet Sci. Lett. 238, 217–224.

Mahsoub, M., Abulnasr, R., Boukhary, M., Faris, M., Abd El Aal, M., 2012. Bio-and sequence stratigraphy of upper cretaceous–palaeogene rocks, east Bahariya concession, Western Desert, Egypt. Geol. Croat. 65, 109–138.

Makris, J., Rihm, R., 1991. Shear-controlled evolution of the Red Sea: pull apart model. Tectonophysics 198, 441–466.

Mart, Y., Hall, J.K., 1984. Structural trends in the northern Red Sea. J. Geophys. Res. Solid Earth 89, 11352–11364.

Mart, Y., Ross, D.A., 1987. Post-Miocene rifting and diapirism in the northern Red Sea. Mar. Geol. 74, 173–190.

Masini, E., Stockli, D., Gómez-Romeu, J., Ball, P., Kusznir, N.J., Calassou, S., 2020. Exploration Challenges and Perspectives of Hyper-Extended Rift Systems: A Northern Red Sea Viewpoint. AAPG Middle East Region Geoscience Technology Workshop. Rift Basin Evolution and Exploration.

McClay, K.R., 1996. Recent advances in analogue modelling: uses in section interpretation and validation. Geological Society, London, Special Publications 99, 201–225.

McClay, K.R., Scott, A.D., 1991. Experimental models of hangingwall deformation in ramp-flat listric extensional fault systems. Tectonophysics 188, 85–96.

McKenzie, D.P., Davies, D., Molnar, P., 1970. Plate tectonics of the Red Sea and east africa. Nature 226, 243–248.

Miller, P.M., Barakat, H., 1988. Geology of the safaga concession, northern Red Sea, Egypt. Tectonophysics 153, 123–136.

Mitchell, N.C., Park, Y., 2014. Nature of crust in the central Red Sea. Tectonophysics 628, 123–139.

Mitchell, N.C., Ligi, M., Ferrante, V., Bonatti, E., Rutter, E., 2010. Submarine salt flows in the central Red Sea. Bulletin 122, 701–713.

Mitchell, N.C., Ligi, M., Feldens, P., Hübscher, C., 2017. Deformation of a young salt giant: regional topography of the R ed S ea M iocene evaporites. Basin Res. 29, 352–369.

Mitchell, N.C., Ligi, M., Rasul, N.M.A., 2019. Variations in Plio-Pleistocene Deposition in the Red Sea. Geological Setting, Palaeoenvironment and Archaeology of the Red Sea. Springer, pp. 323–339.

Mitchell, N.C., Shi, W., Izzeldin, A.Y., Stewart, I.C.F., 2021. Reconstructing the level of the central Red Sea evaporites at the end of the Miocene. Basin Res. 33, 1266–1292.

Mitchell, N.C., Hernandez, K., Preine, J., Ligi, M., Augustin, N., Izzeldin, A., Hübscher, C., 2022. Early stage diapirism in the Red Sea deep-water evaporites: origins and length-scales. Tectonophysics 831, 229331.

Mohriak, W., 2014. Birth and Development of Continental Margin Basins: Analogies from the South Atlantic, North Atlantic, and the Red Sea. AAPG Search Discov. Artic 41502.

Mohriak, W., 2019. Rifting and salt deposition on continental margins: differences and similarities between the Red Sea and the South Atlantic sedimentary basins. Geological Setting, Palaeoenvironment and Archaeology of the Red Sea 159–201.

Montenat, C., D'Estevou, P.O., Purser, B., Burollet, P.-F., Jarrige, J.-J., Orszag-Sperber, F., Philobbos, E., Plaziat, J.-C., Prat, P., Richert, J.-P., 1988. Tectonic and sedimentary evolution of the gulf of Suez and the northwestern Red Sea. Tectonophysics 153, 161–177.

Moustafa, A.R., Khalil, S.M., 2020. Structural Setting and Tectonic Evolution of the Gulf of Suez, NW Red Sea and Gulf of Aqaba Rift Systems. The Geology of Egypt. Springer, pp. 295–342.

Muzaffar, A., Keller, J., Borsato, R., 2018. Structural Characterization of the Middle Miocene Mansiyah Salt in the Red Sea. EGU General Assembly Conference Abstracts, p. 2202.

Nilsen, K.T., Vendeville, B.C., Johansen, J.-T., 1995. Influence of Regional Tectonics on Halokinesis in the Nordkapp Basin. Barents Sea.

Orszag-Sperber, F., Harwood, G., Kendall, A., Purser, B.H., 1998. A Review of the Evaporites of the Red Sea-Gulf of Aden. Sedimentation and Tectonics in Rift Basins Red Sea:-Gulf of Aden. Springer, pp. 409–426.

Patton, T.L., Moustafa, A.R., Nelson, R.A., Abdine, S.A., 1994. Tectonic Evolution and Structural Setting of the Suez Rift: Chapter 1: Part I. Type Basin. Gulf of Suez.

Pichel, L.M., Peel, F., Jackson, C.A.L., Huuse, M., 2018. Geometry and kinematics of salt-detached ramp syncline basins. J. Struct. Geol. 115, 208–230.

Pichel, M., Finch, E., Gawthorpe, R.L., 2019. The impact of pre-salt rift topography on salt tectonics: a discrete-element modeling approach. Tectonics 38, 1466–1488.

Richter, H., Makris, J., Rihm, R., 1991. Geophysical observations offshore Saudi Arabia: seismic and magnetic measurements. Tectonophysics 198, 297–310.

Rihm, R., Makris, J., Möller, L., 1991. Seismic surveys in the Northern Red Sea: asymmetric crustal structure. Tectonophysics 198, 279–295.

Rojo, L.A., Escalona, A., 2018. Controls on minibasin infill in the Nordkapp Basin: evidence of complex Triassic synsedimentary deposition influenced by salt tectonics. AAPG Bull. 102, 1239–1272.

Rojo, L.A., Cardozo, N., Escalona, A., Koyi, H., 2019. Structural style and evolution of the Nordkapp Basin, Norwegian Barents Sea. AAPG Bull. 103, 2177–2217.

Rojo, L.A., Koyi, H., Cardozo, N., Escalona, A., 2020. Salt tectonics in salt-bearing rift basins: progradational loading vs extension. J. Struct. Geol. 141, 104193.

Ross, D.A., Schlee, J., 1973. Shallow structure and geologic development of the southern Red Sea. Geol. Soc. Am. Bull. 84, 3827–3848.

Rowan, M.G., 2014. Passive-margin salt basins: hyperextension, evaporite deposition, and salt tectonics. Basin Res. 26, 154–182.

Saleh, S., Jahr, T., Jentzsch, G., Saleh, A., Abou Ashour, N.M., 2006. Crustal evaluation of the northern Red Sea rift and Gulf of Suez, Egypt from geophysical data: 3-dimensional modeling. J. Afr. Earth Sci. 45, 257–278.

Schettino, A., Macchiavelli, C., Pierantoni, P.P., Zanoni, D., Rasul, N., 2016. Recent kinematics of the tectonic plates surrounding the Red Sea and gulf of aden. Geophys. J. Int. 207, 457–480.

Schettino, A., Macchiavelli, C., Rasul, N.M.A., 2019. Plate motions around the Red Sea since the early Oligocene. Geological Setting, Palaeoenvironment and Archaeology of the Red Sea 203–220.

Smith, J.E., Santamarina, J.C., 2022. Red sea evaporites: formation, creep and dissolution. Earth Sci. Rev., 104115

Sultan, M., Becker, R., Arvidson, R.E., Shore, P., Stern, R.J., El Alfy, Z., Guinness, E.A., 1992. Nature of the Red Sea crust: a controversy revisited. Geology 20, 593–596.

Tewfik, N., Ayyad, M., 1982. Petroleum exploration in the Red Sea shelf of Egypt. In: Proc. 6th Exploration Seminar, Egyptian General Petroleum Corporation and Egypt Petroleum Exploration Society, pp. 159–180. Cairo.

Tubbs, R.E., Fouda, H.G.A., Afifi, A.M., Raterman, N.S., Hughes, G.W., Fadolalkarem, Y. K., 2014. Midyan Peninsula, northern Red Sea, Saudi Arabia: seismic imaging and regional interpretation. GeoArabia 19, 165–184.

van Hinsbergen, D.J.J., De Groot, L.V., van Schaik, S.J., Spakman, W., Bijl, P.K., Sluijs, A., Langereis, C.G., Brinkhuis, H., 2015. A paleolatitude calculator for paleoclimate studies. PLoS One 10, e0126946.

Vendeville, B.C., Jackson, M.P.A., 1992a. The rise of diapirs during thin-skinned extension. Mar. Petrol. Geol. 9, 331–354.

Vendeville, B.C., Jackson, M.P.A., 1992b. The fall of diapirs during thin-skinned extension. Mar. Petrol. Geol. 9, 354–371.

Warren, J.K., 2010. Evaporites through time: tectonic, climatic and eustatic controls in marine and nonmarine deposits. Earth Sci. Rev. 98, 217–268.

Withjack, M.O., Callaway, S., 2000. Active normal faulting beneath a salt layer: an experimental study of deformation patterns in the cover sequence. AAPG (Am. Assoc. Pet. Geol.) Bull. 84, 627–651.

Withjack, M.O., Olson, J., Peterson, E., 1990. Experimental models of extensional forced folds. AAPG Bull. 74, 1038–1054.